Title

The roles of depth varying mechanical properties and permeability of the deep boundary condition in confined compression of articular cartilage

Author

Lee, John J.

Publication Date

2011

UNIVERSITY OF CALIFORNIA, SAN DIEGO

THE ROLES OF DEPTH VARYING MECHANICAL PROPERTIES AND PERMEABILITY OF THE DEEP BOUNDARY CONDITION IN CONFINED COMPRESSION OF ARTICULAR CARTILAGE

A thesis submitted in partial satisfaction of the

requirements for the degree Master of Science

in

Bioengineering

by

John J. Lee

Committee in charge:

Professor Robert L. Sah, Chair
Professor Koichi Masuda
Professor Jeffrey H. Omens

2011

The thesis of John J. Lee is approved, and it is acceptable in quality and form for publication on microfilm and electronically:

Chair

University of California, San Diego

2011

TABLE OF CONTENTS

LIST OF FIGURES

ACKNOWLEDGMENTS

I would like to acknowledge support by the National Institute of Health through the Short Term Research Training Grants in 2005 and 2006.

I would like to acknowledge my colleagues in the lab, Drs. Albert Chen, Chad Lewis, Won Bae and Benjamin Wong for providing the technical expertise and mentoring that made any of this possible.

ABSTRACT OF THE THESIS

THE ROLES OF DEPTH VARYING MECHANICAL PROPERTIES AND PERMEABILITY OF THE DEEP BOUNDARY CONDITION IN CONFINED COMPRESSION OF ARTICULAR CARTILAGE

by

John J. Lee

Master of Science in Bioengineering

University of California, San Diego, 2011

Professor Robert L. Sah, Chair

Articular cartilage has depth-varying composition and structure that are manifest as depth-varying biomechanical properties. In addition, the subchondral bone region has a hydraulic permeability which is markedly increased in osteoarthritis. Thus, the effects of the depth-varying properties of articular cartilage and of the permeability of the deep boundary on the biomechanical behavior of cartilage were determined for oscillatory confined compression both experimentally and using a poroelastic multi-layer model. Homogeneous (**a**) and inhomogeneous (**b**) sample structures were both experimentally tested as well as simulated in two confined compression testing setups, one with an impermeable base (**I**) and a freely-permeable base (**II**) at 15% offset. The model and experimental results demonstrate that the high

modulus and low permeability of the deep layer of cartilage normally provide a sealing effect, such that fluid pressurization and dynamic stiffness are maintained much more similarly for conditions **Ib** and **IIb** than for conditions **Ia** and **IIa**, with these differences between **I** and **II** diminishing at lower frequencies for both sample structures. In the simulation, strain and solid stress were more distributed throughout the sample depth and propagated deeper into the tissue from permeable boundary conditions in **Ia** and **IIa** than in **Ib** and **IIb**. In summary, the depth varying properties of the inhomogeneous sample and an impermeable deep boundary provide increased fluid pressurization capability that when combined have a cumulative effect, effectively shielding the tissue from large strain and stress levels.

CHAPTER 1

INTRODUCTION

1.1 General Introduction to the Thesis

It has been well established that articular cartilage is an inhomogeneous biological material consisting of a fluid phase with electrolytes and a solid phase primarily consisting of collagen and proteoglycan [1-8]. The orientation of collagen is known to change with depth from a more parallel orientation to the articular surface superficially to a perpendicular orientation in the deep layers. Proteoglylcan concentration is known to increase with depth [1, 9-13]. Several biomechanical studies have shown that the compressive modulus of full thickness cartilage can vary 30 fold or more from superficial to deep while tissue permeability has been shown to decrease with depth [14-17]. Fluorescently labeled chondrocyte nuclei tracked in confined compression showed that the majority of the compression occurs superficially, while the deepest layers show no significant compression [16, 17]. It has yet to be determined what the role of this inhomogeneity is in terms of the tissue's dynamic mechanical response. Biphasic cartilage tissue models have shown that the inhomogeneity of cartilage produces a distribution of stresses and strains within the tissue in response to loads [4]. The inhomogeneous stress-strain state provides a clue to the structure-function relationship in healthy articular cartilage [18]. Furthermore it is well known that chondrocyte biosynthetic activity depends on the surrounding electromechanical milieu [19]. When pathological changes occur in cartilage as in arthritis, the electromechanical milieu is altered, affecting the biological response as well as the biomechanical response of the tissue. In addition, the subchondral bone plate's (ScBP) role in the overlying cartilage's mechanical response is unknown. Subchondral bone plate changes have been well documented in pathological conditions and a change in permeability may provide a significant route of exit for fluid exudation during cartilage compression [20-30]. The overall objective of this present study is to determine what role the inhomogeneity of cartilage and the permeability of the boundary condition have in the biomechanical response of the tissue.

1.2 Structure, Composition, and Function of Articular Cartilage

Hyaline articular cartilage is composed of an extracellular matrix (ECM) with a small number of specialized chondrocytes distributed throughout. The ECM is composed primarily of negatively charged proteoglycans (PGs) and collagen with small amounts of other proteins and glycoproteins and is infiltrated with water and its constituent ions, primarily Na^+ and Cl^-. By wet weight, 65 to 80% of cartilage is water [6,34]. This water is distributed inhomogeneously with depth having the highest concentration near the surface at 80% and decreasing to 65% in the deepest layers near the subchondral bone [40]. Nearly 75% of the dry weight of cartilage is collagen, of which 90 to 95% is type II, and about 20-30% of the dry weight of cartilage is proteoglycan. Collagen is assembled into small and large fibrils that have an orientation, dimension, and concentration that vary with depth [1, 9, 10, 36, 37]. Proteoglycans, in contrast, are biomacromolecules consisting of a protein core with numerous glycosaminoglycan (GAG) side chains. These GAG side chains contain at least one negatively charged group, a carboxyl and/or a sulfate [41, 42], that as a group constitute the high-net negative charge density of the aggrecan, referred to quantitatively as the fixed charge density (FCD) [34, 43]. Most of these aggrecan molecules are bound to a single hyaluronan chain to form large PG aggregates of 50-100 MDa [41, 42]. These complex PG aggregates are self restrained within its intertwined structure and fill the intrafibrillar space to form the solid matrix of cartilage [1, 31, 32, 41].

The matrix of articular cartilage has an ultrastructural arrangement that varies with depth from the articular surface to the underlying subchondral bone. The collagen fibrils in the superficial 10 to 20%, known as the superficial transition or tangential zone (STZ), are predominantly oriented parallel with the articular surface and are densely packed. In addition, this region has relatively low PG content at 10% of dry weight and a relatively low permeability to fluid flow [11], which provides an important barrier for fluid flow during compression [3, 11]. In the next 40 to 60% of the depth, known as the middle or transitional zone, collagen fibers are larger and are either randomly or radially oriented [1, 9, 10, 12, 13]. In this zone, the PG content rises to 25% of dry weight which gives this zone a high swelling pressure from the Donnan osmotic pressure and subsequently a high water content. In cartilage that has a damaged superficial zone, the water content in the middle zone is increased even further [34, 44]. In the deepest 30% of cartilage near the subchondral bone interface, the PG content is relatively low, however, the PG aggregates here are larger and more saturated with aggrecan than in the surface or middle zones. At this depth the collagen fibers form bundles and are larger and oriented perpendicular to the subchondral bone interface [9, 10, 13, 34].

When an external load is applied to cartilage, cartilage deforms to increase contact area and congruence, minimizing contact stress [2, 3, 31, 32]. Cartilage experiences tensile, compressive and shear stresses in a spatially and depth varying manner that is dependent on the structural organization and composition of the tissue. Over the years, cartilage has been predominantly tested in three configurations including confined compression, unconfined compression and indentation tests, with tensile experiments representing a minority of the studies.

Early mechanical testing of cartilage utilized indentation experiments to measure an apparent compressive elastic modulus [45-52]. These experiments usually consisted of a constant step load that was applied to samples with either a plane ended cylinder or an impermeable spherical tip and deformation was measured over time. An instantaneous elastic deformation was followed by creep to an asymptotic deformation. Two moduli were reported, one at or shortly after load application and another after creep deformation. Persistent deformation was found to be reversible in a saline bath with time and revealed that cartilage creep was largely due to the flow of interstitial fluid from the tissue [53]. Eventually the use of porous platens and sinusoidally varying compressive forces near 1 Hz frequency were used to simulate cyclic physiological loads [54]. Using porous platens in uniaxial compression tests revealed an instantaneous and 30 min equilibrium Young's modulus of 11.1 MPa and 0.32 MPa, respectively [55].

In these early studies, cartilage was assumed to behave elastically when samples were loaded fairly quickly. This elasticity assumption only holds when there is no fluid exudation out of the tissue, either immediately after applying load or at equilibrium. Gait analyses have shown that the sequence of loading and unloading occurs within a second and that peak loads are reached within an average of 0.5 seconds [56]. Even more transient, impact loads are applied in milliseconds. This suggests that under most functional and practical situations such as walking or running, the elasticity assumption for cartilage is reasonable and that time dependent viscoelastic behavior may be ignored.

With longer load application times, a multiphasic model with mixed solid and fluid phases has described the compressive viscoelastic properties of cartilage quite well. Understanding cartilage as a multiphasic structure and describing cartilage deformation with relation to fluid flow was originally based on a soil consolidation theory from the early 1940s [57]. This theory conceptualized three phases in soil settling that were carried over to cartilage and other poroelastic tissue mechanics. The first phase is attributed to water flowing out of soil directly beneath the load being applied.

The second phase is described as water flowing from loaded to unloaded regions within the soil and the third phase linked the restraining effect of the unloaded region upon the loaded region. By the early 1960s, McCutchen hypothesized that the fluid phase carried most of the load in cartilage [55] and Zarek and Edwards began conceptualizing cartilage as a biphasic structure consisting of a porous elastic solid matrix saturated with fluid [58]. Load was believed to be carried partly by pressure in the fluid and partly by compressive stresses in the solid matrix. Furthermore, confined compression testing using a porous piston allowing unrestrained flow in the normal direction to the surface showed that the solid matrix could not be modeled accurately as a linearly elastic material, that the matrix itself was viscoelastic [59].

In tension experiments, the collagen fibrils and PG structures are aligned and stretched along the load axis when tensed. Initially, in small deformation, there is a small non linear toe region in the stress-strain curve as the collagen fibrils are being aligned along the axis of load through the PG matrix. After these collagen fibrils are aligned, further deformation causes the collagen fibers to stretch, generating a much larger tensile stiffness due to the stiffness of the collagen fibrils themselves [33, 60-70]. The linear region of the tensile stress-strain curve gives the intrinsic tensile equilibrium Young's modulus of the tissue which has been measured in the range of 5-25 MPa, depending on the depth and orientation and the location of the joint where the sample was obtained, illustrating the inhomogeneity and anisotropy of cartilage. Superficial tangential zone cartilage is much stiffer than middle and deep zone cartilage [33, 60-63, 70]. The stiffness, also depends on orientation, with tensile stiffness greater parallel to the local split line direction. These split lines indicate the orientation of collagen fibers [1, 33, 60-63]. For humans, articular cartilage tensile stiffness decreases with age [33, 63, 66, 67].

1.3 Biphasic, Triphasic and Quadriphasic Mixture Theories of Articular Cartilage

In 1980 the biphasic mixture theory was introduced to model articular cartilage as a two phase structure consisting of an incompressible fluid phase and an incompressible porous permeable solid phase [1-7, 71]. Early studies had shown that the viscoelastic behavior of cartilage is related to interstitial fluid flow and exudation and this biphasic model, for the first time, was able to describe the stress-strain behavior of cartilage utilizing interstitial fluid flow and pressurization and an intrinsic compressive mechanical property for the solid matrix. A major concept missed in earlier cartilage compression studies was that the interstitial fluid flow and its frictional drag against the solid matrix, which account for the viscoelastic behavior, obscured the true measurement of the intrinsic solid matrix mechanical properties which can only be determined at equilibrium. This model has been used in a variety of experiments including confined compression [1, 2, 4, 14, 38, 72-74], unconfined compression [68, 69, 75-79], in situ indentation testing [6, 80-86], contact analysis of articulating cartilage surfaces [1, 7, 31, 87-90], and chondrocyte-matrix interaction under mechanical loading [86, 91-93].

The biphasic mixture theory correlates viscoelastic physical mechanisms with observed mechanical behavior well. When cartilage tissue is compressed, fluid is exuded from the tissue giving rise to a loss of volume. The creep response can be explained by a rapid fluid flow phase initially followed by gradually diminishing flow as permeability decreases with increasing strain until flow stops and the compressive stress within the solid matrix balances the applied stress, reaching equilibrium. The load applied during creep at the surface is balanced by compressive stress developed within the solid matrix and by frictional drag generated by interstitial fluid flow. For thick human cartilage up to 4 mm, the creep response can take 4 to 16 hours to reach equilibrium [6]. The time to reach equilibrium is inversely related to the square of the tissue thickness. On the other hand, during stress relaxation, compressive stress rises due to fluid pressurization initially due to the limited permeability of the matrix. Subsequent stress relaxation is accounted for by fluid exudation and redistribution within the matrix. This relaxation ceases when the compressive stress equals the equilibrium stress determined by the aggregate compressive modulus of the matrix. There is a linear relationship between equilibrium stress and strain up to about 20% strain [4-6]. However for larger strains, a nonlinear stiffening effect can be seen in uniaxial compression tests on cylindrical cartilage specimens with values ranging from 12 to 45 MPa with increasing strain, effectively limiting the compressive strain sustained by the tissue under large loads [94]. In physiological loading conditions characterized by low strain rates, high stress levels are difficult to maintain because stress relaxation occurs so rapidly. This allows for necessary rapid spreading of the contact area in the joint during articulation. When the compressive load is removed, cartilage will re-expand to its initial volume through a combination of the matrix elasticity, increased Donnan osmotic pressure secondary to an increased FCD within the tissue and imbibition and redistribution of fluid [1, 4-7, 53, 54].

One study has shown that in the hip, compressive stresses as high as 20 MPa can occur [95]. Cartilage can withstand such pressures because the extremely small permeability of cartilage allows large interstitial fluid pressurization during compression. This effectively shields the solid matrix from high stresses and strains during joint loading [1, 73, 96]. In confined compression experiments where the interstitial fluid pressure was measured simultaneously at the articular surface, the interstitial fluid was immediately pressurized with loading and accounted for greater than 95% of the load support [73, 96]. Furthermore, it was shown that this high load support by the fluid can last more than 500 seconds because of a large viscoelastic characteristic time constant, τ. In all practicality, the interstitial fluid pressurization acts to protect the solid matrix in most daily functions of living.

The biphasic theory has been sufficiently accurate in explaining much of the observed mechanical behavior of articular cartilage in compression. However, in conditions where there is no fluid exudation out of the tissue including abrupt load applications and high strain rate conditions, the biphasic theory does not do so well in explaining the immediate response in these conditions. In these cases, it is reasonable to assume that cartilage behaves as a simple single phase linear elastic solid as was done in the early studies of cartilage. Eberhardt has presented some arguments using experimental data for the use of a linear elastic model to study cartilage failure [97].

Building on the biphasic theory, the triphasic theory separates the interstitial mobile ions as a separate contributing phase in the mechanoelectrochemical behavior of cartilage [40]. The fixed negative charges of the PGs attract counter cations in the interstitial fluid that give rise to the Donnan osmotic swelling pressure. These ions have been found to play an integral role in the mechanoelectrochemical response of cartilage under loading [1, 34, 43, 77, 98-110]. As a further refinement, a quadriphasic theory was developed [105] where the two predominant ions in the interstitial fluid, Na^+ and Cl^-, are considered two phases, instead of one as in the triphasic theory. Both theories have been used to describe flow-dependent and flow-independent viscoelastic, swelling, and electrokinetic behavior of cartilage [1, 40, 74, 77, 98, 101, 105-107, 111]. The triphasic theory has been able to determine the electrokinetic coefficients and physical parameters associated with the FCD, concentration of the ions, and frictional coefficients between ions/fluid and the solid matrix [40, 74, 99, 100, 111].

In stress relaxation tests, the triphasic theory results show that the equilibrium aggregate modulus consists of the Donnan osmotic swelling pressure and the intrinsic stiffness of the solid matrix. The Donnan osmostic swelling pressure contributes up to about 50% of the equilibrium confined compression stiffness and about 30% of the equilibrium unconfined compression stiffness [74-77]. The triphasic model also tells us that the fluid pressure is a combination of the hydrodynamic fluid pressure and the Donnan osmotic pressure. In confined compression the fluid pressure is equal to the osmotic pressure in situations where there is no fluid flow or exudation from the tissue, specifically at equilibrium and prior to load application.

The triphasic theory also elucidated the two sources of electrical potential within cartilage: the diffusion potential from the inhomogeneous distribution of the FCD and the streaming potential from fluid flow convection within charged tissue. These two sources have opposite polarity and depend not only on the FCD and its distribution but also on the intrinsic Young's modulus, Poisson's ratio and permeability [111]. Depending on whether the tissue is soft like in osteoarthritis or stiff like in normal cartilage, the potential is predominately diffusion related or streaming potential related, respectively [111].

To maintain electroneutrality within cartilage, the negative charges of the PGs are balanced with mobile cations (i.e., Na+) that are dissolved in the interstitial fluid. The result is an imbalance of mobile ions between the cartilage interstitial fluid and the bathing solution that gives rise to the Donnan osmotic swelling pressure [34, 40, 74, 111-115]. In equilibrium, this swelling pressure is balanced by the tensile forces in the matrix or more specifically by the collagen network [34, 114]. In physiological conditions, the cartilage matrix is in a state of pre-stress, balancing this osmotic swelling pressure and determining the volume of the tissue. Changing the internal GAG content or altering the concentration of ions in the bathing solution will alter the internal swelling pressure and the volume of the tissue. To illustrate this concept, studies of samples of cartilage weighed immediately after equilibration in 0.015 M NaCl compared with 0.15 M NaCl illustrated large weight gains in the samples bathed in 0.015 M NaCl, with the largest weight gain observed in the middle zone where the FCD is largest. When these cartilage samples were subjected to collagenase treatment, the weight gain in a hypotonic solution was even larger due to the loosening of the collagen network and subsequent decrease in the tensile stiffness of the tissue [115-117], illustrating the role of the collagen network in resisting swelling pressure. In OA, studies have shown that cartilage tissue has increased hydration and decreased PG in the early stages [1, 2, 33-35, 63, 112, 116, 117]. Swelling behaviors have also been observed in isometric tensile and compressive tests where cartilage samples are held at a constant length with an initial tensile or compressive strain and transient forces are measured when the sample is subjected to hypotonic solutions [33, 40, 63, 118, 119].

1.4 Cartilage Constitutive Modelling and Computation

Since the 1940s, there have been many constitutive theories for cartilage tissue mechanics including both linear and nonlinear elasticity and viscoelasticity [69, 120-122] theories and infinitesimal [2, 4, 71] and finite deformation [94, 123, 124] theories. Material anisotropies and inhomogeneities have also been investigated. Today, the multiphasic porous media theories predominate the literature [4-6, 14, 15, 71-74, 77, 91, 96, 99, 100, 107, 111, 125]. The two continuum theories commonly used today are the biphasic mixture theory [1, 4-6, 71-73, 91, 96, 126] and the two multiphasic mixture theories, triphasic and quadriphasic [40, 74, 77, 94, 99, 100, 107, 111, 125]. In addition, finite element models using the biphasic theory have been applied to indentation and unconfined compression tests [31, 87, 93, 127-132].

These constitutive models made it possible to determine the intrinsic compressive properties of cartilage. Using either a stress-relaxation or creep test in confined compression, two intrinsic properties could be estimated using an isotropic homogeneous biphasic constitutive theory: 1) the equilibrium confined compression modulus, H_A, with units of MPa and 2) the hydraulic permeability, k, in units of m^2/Pa s [4]. A time constant, τ, defined by the compressive modulus, H_A, permeability, k, and the thickness of the sample, h, describes the time course of the viscoelastic transient responses in stress-relaxation and creep: $\tau = h^2/H_A k$. With the previously determined equilibrium compressive aggregate modulus, H_A, the hydraulic permeability can be determined from time-dependent deformational behavior. The equilibrium compressive aggregate modulus has been reported in the range of 0.1-2.0 MPa for all types of articular cartilage and the hydraulic permeability in the range of $1.2\text{-}1.6 \times 10^{-16}$ m^2/Pa s. There is a linear relationship between equilibrium stress and strain up to about 20% strain [4-6]. However for larger strains, a nonlinear stiffening effect can be seen in uniaxial compression tests on cylindrical cartilage specimens with values ranging from 12 to 45 MPa with increasing strain, effectively limiting the compressive strain sustained by the tissue under large loads [94].

Using video microscopy to track fluorescently labeled chondrocyte nuclei as fiducial markers, the depth varying equilibrium compressive aggregate modulus has been determined [14-17]. Using the strain fields developed from the videos and the isotropic inhomogeneous biphasic model, intrinsic aggregate modulus ranged from 1.16 MPa in the superficial layer to 7.75 MPa in the deep layer [14]. This was taken a step further with an optimized digital image correlation technique and the triphasic model to determine a continuous depth-dependent distribution of the aggregate modulus and FCD [14, 15, 133]. The FCDs determined with this method compare very favorably with the biochemical analyses of the three zones [34, 115].

Interstitial fluid flow due to compression of cartilage is determined by the hydraulic permeability of the solid matrix. This permeability is determined by the matrix pore structure, size, and connectivity [1, 4-7, 34, 43, 71, 72, 98-100, 126, 134]. In addition, the negative charge of PGs affects tissue permeability as the negative charge density impedes fluid flow through an electro-osmosis phenomenon [1, 34, 71, 99, 100]. A nonlinear strain dependent permeability function was developed by Lai et al to model the decrease in permeability with increasing strain which causes the pores themselves to compact to a smaller size and increases the FCD, further impeding fluid flow. The permeability constitutive law, $k = k_0 e^{M\varepsilon}$, consists of an intrinsic permeability coefficient at zero strain, k_0, a dimensionless nonlinear interaction coefficient, M, and strain, ε [5]. The effects of nonlinear strain-dependent permeability and the rate of compression on cartilage compression behavior showed that when the strain rate is really small, the fluid flow effects become negligible, and for large M values and high strain rates, large instantaneous compressive stresses several times higher than at equilibrium are predicted [135].

The biphasic mixture theory has been very successful in describing confined compression behavior, but the early isotropic homogeneous biphasic mixture model had some difficulty with the viscoelastic behavior of cartilage in unconfined compression and in indentation tests [14, 77, 78, 125]. Incorporating the inhomogeneous, non-linear, and anisotropic material properties into the model has enhanced the biphasic models ability to describe the electromechanical behavior of cartilage [14-17, 60-63, 69, 78, 79, 91, 103, 104, 118, 120, 121, 125, 132, 136-138]. The inclusion of transverse isotropy material properties into the linearly elastic homogeneous biphasic model improved the predictive power in unconfined compression and in the contact problem [87, 132, 137]. The inclusion of intrinsic matrix viscoelastic properties also improved the biphasic model's predictive power in unconfined compression [3, 59, 68, 69, 78, 79, 120, 121]. The incorporation of a tensile fibrous microstructure into the linearly elastic biphasic theory further refined the biphasic theory's predictive power, specifically in unconfined compression [139-141]. Recent studies have also included a conewise tension compression nonlinearity, which accounts for a nearly two orders of magnitude difference in tensile and compressive moduli, [120] and intrinsic viscoelasticity [139], improving the accuracy in modeling articular cartilage deformation in multiple testing configurations. These additional enhancements also did well in predicting the fluid pressure in confined compression [73, 96].

In unconfined compression stress-relaxation or creep tests, the intrinsic equilibrium Young's modulus, E, Poisson's ratio, ν, and hydraulic permeability, k, can be determined with an isotropic homogeneous biphasic model or a finite element formulation of an isotropic triphasic mixture theory [4, 75, 77]. The biphasic mixture theory is similar to the single-phase isotropic homogeneous linear elasticity theory in that there are only two independent intrinsic equilibrium constants, the Young's modulus, E, and Poisson's ratio, ν. The shear modulus, μ, and aggregate modulus, H_A, are related to these two constants by the following relationships:

$$\mu = \frac{E}{2(1+\nu)} \quad (2.1.1)$$

$$H_A = \frac{E(1-\nu)}{(1+\nu)(1-2\nu)} \quad (2.2.2)$$

The intrinsic equilibrium Young's modulus is determined at equilibrium in the stress relaxation test. Poisson's ratio can be determined by an optical method in unconfined compression testing, measuring the lateral expansion at equilibrium during stress-relaxation or creep test or can be calculated using a master solution from the biphasic indentation test [6, 75, 76]. The equilibrium Young's compression modulus has been reported in the range of 0.41 to 0.85 MPa and the equilibrium Poisson's ratio in the range of 0.06 to 0.18 [76, 80-84]. Furthermore, the finite element formulation of an isotropic triphasic mixture theory revealed that the apparent Poisson's ratio is greater than the intrinsic Poisson's ratio of an equivalent uncharged ECM because of the Donnan osmotic swelling pressure [77]. The apparent Young's modulus is greater than the intrinsic Young's modulus of an equivalent uncharged ECM, again revealing that the apparent Young's modulus, similar to the Poisson's ratio, depends not only on the intrinsic solid matrix Young's modulus but also on the FCD and the intrinsic Poisson's ratio.

The stress strain fields from indentation tests of cartilage are much more complex than the previously mentioned confined and unconfined compression tests. The advantage of using an indentation test is that it is minimally disruptive of the cartilage tissue and has the potential to be used in vivo. Despite the complexity of this problem, constitutive laws have been formulated for this type of testing. Using an isotropic homogeneous biphasic theory, the equilibrium aggregate modulus, H_A, Poisson's ratio, ν, and hydraulic permeability, k, can be determined simultaneously [6, 48, 50, 51, 82, 129]. The range of values for these intrinsic properties are similar to the ones measured using confined and unconfined compression setups providing not only confidence in the experimental methods but also in the biphasic theory itself: H_A, 0.4-0.9 MPa; ν, 0.13-0.45; and k, 4-10 x 10^{-16} m^4/Ns.

The dramatic difference between the tensile and compressive elastic properties of cartilage observed thus far was further explored by Huang et al who had performed uniaxial tensile tests of cartilage strips parallel and perpendicular to split line directions and confined compression tests along the depth direction of human glenohumeral cartilage [68, 69, 142]. Near 0% strain, the equilibrium tensile modulus of the humeral head STZ averaged greater than 6.5 MPa along the split line direction and 4.5 MPa perpendicular to this direction. The equilibrium compressive modulus on the other hand averaged 0.5 MPa. At higher tensile strains, the equilibrium tensile modulus was as high as 45 and 25 MPa, parallel and perpendicular to local split line directions, respectively. A conewise biphasic model has been developed that provides remarkable accuracy in describing this order of magnitude tension compression nonlinearity [68, 69, 120, 121, 142]. This data suggests that the elastic material symmetry is at least orthotropic, with three planes of symmetry defined in situ by the split line direction in the plane of the articulating surface, perpendicular to the split line direction, and in the depth direction. Studies also support anisotropy in tension when measuring Poisson's ratio in uniaxial tension [69]. The anisotropy of cartilage in compression however has had limited investigation. Using the conewise tension compression nonlinear biphasic model and a new optical technique, Wang et al tested small cubic cartilage specimens in three directions [143]. The experiments revealed that the Young's modulus and Poisson's ratio were different along each direction.

The biphasic theory is unsuccessful at predicting tensile viscoelastic behavior [33, 60, 67]. Cartilage displays tension-compression nonlinearity and flow independent viscoelasticity [61, 65]. The predictions of the biphasic conewise linear elasticity model are poor for the viscoelastic response in uniaxial tension [68]. These results suggest that the flow-independent viscoelasticity of the solid matrix [3, 65, 144-146] must be manifesting its known viscoelastic behavior during tensile tests [68, 69]. The microstructure of cartilage provides the explanation for this. As cartilage is loaded in tension, the collagen fibers are being stretched, while in compression fluid pressurization and flow is the primary load bearer. This also explains why the biphasic model with solid matrix viscoelasticity better predicts the unconfined compression response. With the development of a biphasic conewise elasticity quasi-linear viscoelasticity (biphasic CLE-QLV) theory can predict cartilage tensile responses extremely well in addition to confined and unconfined compression responses [68, 69]. With these added levels of sophistication, the biphasic model can describe a variety of responses in varying testing configurations helping confirm that the tissue is a mixture type material with nonlinear, viscoelastic, anisotropic characteristics.

1.5 Subchondral Bone - Role in Cartilage Biomechanics

Underlying articular cartilage is a support structure known as the subchondral bone plate which consists of a transitional zone, known as calcified cartilage, and subchondral bone. Just deep to the deep zone of articular cartilage is a structure called the tidemark which separates the uncalcified cartilage from calcified cartilage and marks the beginning of the subchondral bone plate [147]. The background information provided in the previous sections is primarily focused on the uncalcified articular cartilage that rises above the tidemark. Calcified cartilage is vascular [148, 149], while uncalcified cartilage is avascular, and consists of hypertrophic chondrocytes surrounded by a calcified matrix. Structurally, this layer attaches uncalcified cartilage to subchondral bone [150, 151]. It is believed that this layer provides a transitional zone of intermediate stiffness somewhere between uncalcified cartilage and subchondral bone minimizing stress concentrations at the osteochondral interface [152]. Deep to the calcified cartilage is the cement line which represents the ossification front and marks the beginning of the subchondral bone. Unfortunately, not much is known about the biomechanical role of this calcified layer in cartilage degeneration.

Recently there has been an interest in studying the subchondral bone's role in the biomechanics of articular cartilage [20, 153]. It has been largely assumed for decades that the subchondral bone plate is an impermeable barrier to fluid flow and allows the overlying cartilage to maximally pressurize its interstitial fluid to protect the cartilage matrix and chondrocytes from excessive loads. The fluid transport properties of the zone of calcified cartilage at the osteochondral junction, or tidemark, remains largely unknown. Cartilage nutrition studies considered calcified cartilage as an impermeable barrier to material transport from the subchondral bone, especially after joint maturation [154-156]. A more recent in vivo magnetic resonance imaging study has shown that intravenous Gd-DTPA2 crosses the osteochondral interface into uncalcified cartilage [157]. In intervertebral discs studied ex vivo, fluid was shown to flow through vascular channels between the marrow cavity and the cartilaginous disc [158]. These more recent studies suggest that the subchondral bone plate may play an important role in articular cartilage mechanics by allowing fluid flow through the osteochondral interface.

Changes in the subchondral bone plate have been observed in joint degeneration and these include increasing thickness with formation of new zones of calcified cartilage from previously uncalcified cartilage, duplications of the tidemark, and vascular invasion into the tidemark [21, 22, 151]. It is thought that microcracks that develop between the bone marrow space and calcified cartilage from repeated loading may provide the impetus for vascular invasion [23-28]. This vascular invasion may significantly alter the hydraulic permeability of the subchondral bone plate and the mechanoelectrochemical environment of articular cartilage in ways that promote joint degeneration. In addition, experimental animal models have demonstrated a strong link between the existence of a subchondral bone plate and the quality of spontaneously repaired cartilage. Hyaline-like cartilage was found in areas where there was newly formed subchondral bone plate [159, 160].

An increase in hydraulic conductance of osteochondral tissue and the subchondral bone plate may cause progressive deterioration of cartilage. Articular cartilage’s low permeability allows it to support large loads through interstitial fluid pressurization, allowing for prolonged load support and minimizing solid matrix strain [90]. The duration of this load support by fluid pressurization to reach equilibrium is characterized by a viscoelastic time constant, τ, which is dependent on the tissue thickness, h, permeability, k, compressive modulus, H_A, and it's relationship to these is $\tau = h^2/H_A k$ [75]. For healthy human cartilage with a thickness of 1 cm, compressive modulus, H_A, of 0.5 MPa, and permeability, k_p, of 2×10^{-15} m^2/Pa s, the time constant, τ, is 28 hours, a timescale orders of magnitude larger than most physiological situations. With increased hydraulic conductance of both articular cartilage and the subchondral bone plate, an increase of fluid exudation through the subchondral bone plate will lead to shorter equilibrium times and large deformations, accelerating solid matrix degeneration.

Computational models have been pursued in exploring the effects of a freely permeable defect in the subchondral bone plate. A penalty biphasic model was used to explore the effect of the relatively impermeable subchondral bone plate on the dynamic deformational behavior of the cartilage ECM under a cyclic compressive load. A freely permeable subchondral bone defect 1.5 mm wide allows cartilage to reach steady state faster in oscillatory compression. At steady state, the peak magnitude of the interstitial fluid showed little difference than when the subchondral bone is impermeable. However, the ECM strain was significantly larger when the subchondral bone plate is permeable than in the case when the subchondral bone plate is impermeable, providing a mechanism for ECM degeneration [29]. Furthermore, a 2-D linear biphasic finite element analysis performed to determine articular cartilage deformations, interstitial fluid flow and pressurization, under both uniform and nonuniform hydrodynamic pressure distributions showed that with a perforation in the subchondral bone plate, solid matrix stresses and strains are significantly increased as a consequence of diminished fluid pressurization in the region of the defect [30].

1.6 References

1. Mow VC, Ratcliffe A. Structure and function of articular cartilage and meniscus. In: Mow VC, Hayes WC, eds. Basic Orthopaedic Biomechanics. 2nd ed. New York: Raven Press; 1997:113-78.

2. Armstrong CG, Mow VC. Variations in the intrinsic mechanical properties of human articular cartilage with age, degeneration, and water content. J Bone Joint Surg Am 1982;64-A:88-94.

3. Setton LA, Zhu W, Mow VC. The biphasic poroviscoelastic behavior of articular cartilage: role of the surface zone in governing the compressive behavior. J Biomech 1993;26:581-92.

4. Mow VC, Kuei SC, Lai WM, Armstrong CG. Biphasic creep and stress relaxation of articular cartilage in compression: theory and experiment. J Biomech Eng 1980;102:73-84.

5. Lai WM, Mow VC. Drag-induced compression of articular cartilage during a permeation experiment. Biorheology 1980;17:111-23.

6. Mow VC, Gibbs MC, Lai WM, Zhu WB, Athanasiou KA. Biphasic indentation of articular cartilage-II. A numerical algorithm and an experimental study. J Biomech 1989;22:853-61.

7. Mow VC, Ratcliffe A, Poole AR. Cartilage and diarthrodial joints as paradigms for hierarchical materials and structures. Biomaterials 1992;13:67-97.

8. Mow VC, Holmes MH, Lai WM. Influence of load bearing on the fluid transport and mechanical properties of articular cartilage. In: Helminen HJ, Kiviranta I, Säämänen A-M, Tammi M, Paukkonen K, Jurvelin J, eds. Joint Loading. Bristol: Butterworth; 1987:264-86.

9. Clarke IC. Articular cartilage: a review and scanning electron microscope study. 1. The interterritorial fibrillar architecture. J Bone Joint Surg Br 1971;53(4):732-50.

10. Clark JM. Variation of collagen fiber alignment in a joint surface: a scanning electron microscope study of the tibial plateau in dog, rabbit, and man. J Orthop Res 1991;9:246-57.

11. Muir H, Bullough P, Maroudas A. The distribution of collagen in human articular cartilage with some of its physiological implications. J Bone Joint Surg Br 1970;52(3):554-63.

12. Broom ND, Marra DL. Ultrastructural evidence for fibril-to-fibril associations in articular cartilage and their functional implication. J Anat 1986;146:185-200.

13. Redler I, Mow VC, Zimny ML, Mansell J. The ultrastructure and biomechanical significance of the tidemark of articular cartilage. Clin Orthop Rel Res 1975;112:357-62.

14. Wang CC-B, Hung CT, Mow VC. An analysis of the effects of depth-dependent aggregate modulus on articular cartilage stress-relaxation behavior in compression. J Biomech 2001;34:75-84.

15. Wang CC, Guo XE, Sun D, Mow VC, Ateshian GA, Hung CT. The functional environment of chondrocytes within cartilage subjected to compressive loading: a theoretical and experimental approach. Biorheology 2002;39(1-2):11-25.

16. Schinagl RM, Ting MK, Price JH, Sah RL. Video microscopy to quantitate the inhomogeneous equilibrium strain within articular cartilage during confined compression. Ann Biomed Eng 1996;24:500-12.

17. Schinagl RM, Gurskis D, Chen AC, Sah RL. Depth-dependent confined compression modulus of full-thickness bovine articular cartilage. J Orthop Res 1997;15:499-506.

18. Krishnan R, Park S, Eckstein F, Ateshian GA. Inhomogeneous cartilage properties enhance superficial insterstitial fluid support and frictional properties, but do not provide a homogeneous state of stress. J Biomech Eng 2003;125(3):569-77.

19. Sah RL, Kim YJ, Doong JH, Grodzinsky AJ, Plaas AHK, Sandy JD. Biosynthetic response of cartilage explants to dynamic compression. J Orthop Res 1989;7:619-36.

20. Hwang J, Bae WC, Shieu W, Lewis CW, Bugbee WD, Sah RL. Increased hydraulic conductance of human articular cartilage and subchondral bone plate with progression of osteoarthritis. Arthritis Rheum 2008;58:3831-42.

21. Oettmeier R, Abendroth K, Oettmeier S. Analyses of the tidemark on human femoral heads. II. Tidemark changes in osteoarthrosis--a histological and histomorphometric study in non-decalcified preparations. Acta Morphol Hung 1989;37(3-4):169-80.

22. Dequeker J, Mokassa L, Aerssens J, Boonen S. Bone density and local growth factors in generalized osteoarthritis. Microsc Res Tech 1997;37(4):358-71.

23. Sokoloff L. Microcracks in the calcified layer of articular cartilage. Arch Pathol Lab Med 1993;117:191-5.

24. Mori S, Harruff R, Burr DB. Microcracks in articular calcified cartilage of human femoral heads. Arch Pathol Lab Med 1993;117:196-8.

25. Burr DB, Radin EL. Microfractures and microcracks in subchondral bone: are they relevant to osteoarthrosis? Rheum Dis Clin North Am 2003;29(4):675-85.

26. Berry JL, Thaeleroberdoerster DA, Greenwald S. Subchondral pathways to the superior surface of the human talus. Foot & Ankle 1986;7(1):2-9.

27. Holmdahl DE, Ingelmark BE. The contact between the articular cartilage and the medullary cavities of the bone. Acta Orthop Scand 1950;20(2):156-65.

28. Boyde A, Firth EC. Articular calcified cartilage canals in the third metacarpal bone of 2-year-old thoroughbred racehorses. J Anat 2004;205(6):491-500.

29. Suh JK, Li Z, Woo SL-Y. Dynamic behavior of a biphasic cartilage model under cyclic compressive loading. J Biomech 1995;28:357-64.

30. Mow VC, Bachrach NM, Ateshian GA. The effects of a subchondral bone perforation on the load support mechanism within articular cartilage. Wear 1994;175:167-75.

31. Mow VC, Ateshian GA, Spilker RL. Biomechanics of diarthrodial joints: a review of twenty years of progress. J Biomech Eng 1993;115(4B):460-7.

32. Mow VC, Ateshian GA. Lubrication and wear of diarthrodial joints. In: Mow VC, Hayes WC, eds. Basic Orthopaedic Biomechanics. 2nd ed. New York: Raven Press; 1997:275-315.

33. Akizuki S, Mow VC, Muller F, Pita JC, Howell DS, Manicourt DH. Tensile properties of human knee joint cartilage: II. correlations between weight bearing and tissue pathology and the kinetics of swelling. J Orthop Res 1987;5:173-86.

34. Maroudas A. Physicochemical properties of articular cartilage. 2nd ed. Kent, UK: Pitman Med; 1979.

35. Mankin HJ, Mow VC, Buckwalter JA. Articular cartilage repair and osteoarthritis. Rosemont, IL: Am Acad Orthop Surg; 2000.

36. Eyre DR, Dickson IR, van Ness K. The collagens of articular cartilage. Sem Arthritis Rheum 1991;21,S2:2-11.

37. Clark JM, Simonian PT. Scanning electron microscopy of "fibrillated" and "malacic" human articular cartilage: technical considerations. Microsc Res Tech 1997;37:299-313.

38. Guilak F, Ratcliffe A, Lane N, Rosenwasser MP, Mow VC. Mechanical and biochemical changes in the superficial zone of articular cartilage in canine experimental osteoarthritis. J Orthop Res 1994;12:474-84.

39. Jeffrey JE, Thomson LA, Aspden RM. Matrix loss and synthesis following a single impact load on articular cartilage in vitro. Biochim Biophys Acta 1997;1334:223-32.

40. Lai WM, Hou JS, Mow VC. A triphasic theory for the swelling and deformation behaviors of articular cartilage. J Biomech Eng 1991;113:245-58.

41. Muir H. Proteoglycans as organizers of the intercellular matrix. Biochem Soc Trans 1983;11(6):613-22.

42. Hardingham TE, Fosang AJ. Proteoglycans: many forms and many functions. Faseb J 1992;6:861-70.

43. Maroudas A. Physicochemical properties of cartilage in the light of ion exchange theory. Biophys J 1968;8:575-95.

44. Setton LA, Toyama H, Mow VC. Swelling and curling behaviors of articular cartilage. J Biomech Eng 1998;120:355-61.

45. Bär E. Elasticiatssprufunger der gelenkknorpel. Arch Entwickklungsmech Organ 1926;108:739-60.

46. Coletti JM, Akeson WH, Woo SL-Y. A comparison of the physical behavior of normal articular cartilage and the arthroplasty surface. J Bone Joint Surg Am 1972;54-A(1):147-60.

47. Gocke E. Elastiziatats studien am junger und alten gelenkknorpel. Verh Deutsch Orthop Ges 1927;22:130-47.

48. Hayes WC, Keer LM, Herrmann G, Mockros LF. A mathematical analysis for indentation tests of articular cartilage. J Biomech 1972;5(5):541-51.

49. Hirsch C. A contribution to the pathogenesis of chondromalacia of the patella. Acta Chir Scand 1944;90 Suppl(83):9.

50. Hori RY, Mockros LF. Indentation tests of human articular cartilage. J Biomech 1976;9:259-68.

51. Kempson GE, Freeman MAR, Swanson SAV. The determination of a creep modulus for articular cartilage by indentation tests of the human femoral head. J Biomech 1971;4:239-50.

52. Sokoloff L. Elasticity of aging cartilage. Proc Fedn Am Socs Exp Biol 1966;25:1089-95.

53. Johnson G, Dowson D, Wright V. A new approach to the determination of the elastic modulus of articular cartilage. Ann Rheum Dis 1975;34(Supp):116-17.

54. Elmore S, Sokoloff L, Norris G, Carmeci P. Nature of imperfect elasticity of articular cartilage. J Appl Physiol 1963;18:393-96.

55. McCutchen CW. The frictional properties of animal joints. Wear 1962;5:1-17.

56. Paul J. Forces transmitted by joints in the human body. Proc Inst Mech Eng: Lubrication and wear in living and artificial joints 1967;181:8-15.

57. Biot MA. General theory of three-dimensional consolidation. J Appl Phys 1941;12:155-64.

58. Zarek JM, Edwards J. The stress-structure relationship in articular cartilage. Med Electron Biol Eng 1963;1:497-507.

59. Edwards J. Physical characteristics of articular cartilage. Proc Inst Mech Eng 1967;181:16-24.

60. Kempson GE. Mechanical properties of articular cartilage. In: Freeman MAR, ed. Adult Articular Cartilage. 2nd ed. Tunbridge Wells, England: Pitman Medical; 1979:333-414.

61. Woo S, Akeson W, Jemmott G. Measurements of non-homogeneous directional mechanical properties of articular cartilage in tension. J Biomech 1976;9:785–91.

62. Roth V, Mow VC. The intrinsic tensile behavior of the matrix of bovine articular cartilage and its variation with age. J Bone Joint Surg Am 1980;62-A:1102-17.

63. Akizuki S, Mow VC, Muller F, Pita JC, Howell DS, Manicourt DH. Tensile properties of human knee joint cartilage: I. influence of ionic conditions, weight bearing, and fibrillation on the tensile modulus. J Orthop Res 1986;4:379-92.

64. Kempson GE, Muir H, Pollard C, Tuke M. The tensile properties of the cartilage of human femoral condyles related to the content of collagen and glycosaminoglycans. Biochim Biophys Acta 1973;297:456-72.

65. Schmidt MB, Mow VC, Chun LE, Eyre DR. Effects of proteoglycan extraction on the tensile behavior of articular cartilage. J Orthop Res 1990;8:353-63.

66. Kempson GE. Relationship between the tensile properties of articular cartilage from the human knee and age. Ann Rheum Dis 1982;41:508-11.

67. Kempson GE. Age-related changes in the tensile properties of human articular cartilage: a comparative study between the femoral head of the hip joint and the talus of the ankle joint. Biochim Biophys Acta 1991;1075:223-30.

68. Huang CY, Mow VC, Ateshian GA. The role of flow-independent viscoelasticity in the biphasic tensile and compressive responses of articular cartilage. J Biomech Eng 2001;123(5):410-7.

69. Huang C-Y, Soltz M, Kopacz M, Mow V, Ateshian G. Experimental verification of the role of intrinsic matrix viscoelasticity and tension-compression nonlinearity in the biphasic responses of cartilage in unconfined compression. J Biomech Eng 2003;125:84-93.

70. Woo SL-Y, Akeson WH, Jemmott GF. Measurements of nonhomogeneous directional mechanical properties of articular cartilage in tension. J Biomech 1976;9:785-91.

71. Mow VC, Holmes MH, Lai WM. Fluid transport and mechanical properties of articular cartilage: a review. J Biomech 1984;17:377-94.

72. Holmes MH, Lai WM, Mow VC. Singular perturbation analysis of the nonlinear, flow-dependent compressive stress relaxation behavior of articular cartilage. J Biomech Eng 1985;107:206-18.

73. Soltz MA, Ateshian GA. Experimental verification and theoretical prediction of cartilage interstitial fluid pressurization at an impermeable contact interface in confined compression. J Biomech 1998;31:927-34.

74. Mow V, Ateshian G, Lai W, Gu W. Effects of fixed charges on the stress relaxation behavior of hydrated soft tissue in a confined compression problem. Int J Struct Solids 1998;35:4945-62.

75. Armstrong CG, Lai WM, Mow VC. An analysis of the unconfined compression of articular cartilage. J Biomech Eng 1984;106:165-73.

76. Jurvelin J, Buschmann M, Hunziker E. Optical and mechanical determination of poisson's ratio of adult bovine humeral articular cartilage. J Biomech 1997;30:235–41.

77. Sun D, Guo X, Likhitpanichkul M, Lai W, Mow V. The influence of the fixed negative charges on mechanical and electrical behaviors of articular cartilage under unconfined compression. J Biomech Eng 2002;126:6-16.

78. DiSilvestro MR, Zhu Q, Wong M, Jurvelin JS, Suh JK. Biphasic poroviscoelastic simulation of the unconfined compression of articular cartilage: I--Simultaneous prediction of reaction force and lateral displacement. J Biomech Eng 2001;123(2):191-7.

79. DiSilvestro MR, Zhu Q, Suh JK. Biphasic poroviscoelastic simulation of the unconfined compression of articular cartilage: II--Effect of variable strain rates. J Biomech Eng 2001;123:198-200.

80. Athanasiou KA, Rosenwasser MP, Buckwlter JA, Malinin TI, Mow VC. Interspecies comparisons of in situ intrinsic mechanical properties of distal femoral cartilage. J Orthop Res 1991;9:330-40.

81. Lyyra-Laitinen T, Niinimaki M, Toyras J, Lindgren R, Kiviranta I, Jurvelin JS. Optimization of the arthroscopic indentation instrument for the measurement of thin cartilage stiffness. Phys Med Biol 1999;44(10):2511-24.

82. Lyyra T, Kiviranta I, Vaatainen U, Helminen HJ, Jurvelin JS. In vivo characterization of indentation stiffness of articular cartilage in the normal human knee. J Biomed Mater Res 1999;48(4):482-7.

83. Froimson M, Ratcliffe A, Gardner T, Mow V. Differences in patellofemoral joint cartilage material properties and their significance to the etiology of cartilage surface fibrillation. Osteoarthritis Cartilage 1997;5:377-86.

84. Athanasiou KA, Agarawal A, Dzida FJ. Comparative study of the intrinsic mechanical properties of the human acetabular and femoral head cartilage. J Orthop Res 1994;12:340-9.

85. Kim YJ, Sah RL, Grodzinsky AJ, Plaas AH, Sandy JD. Mechanical regulation of cartilage biosynthetic behavior: physical stimuli. Arch Biochem Biophys 1994;311:1-12.

86. Guilak F, Ratcliffe A, Mow VC. Chondrocyte deformation and local tissue strain in articular cartilage: a confocal microscopy study. J Orthop Res 1995;13:410-21.

87. Donzelli PS, Spilker RL, Ateshian GA, Mow VC. Contact analysis of biphasic transversely isotropic cartilage layers and correlations with tissue failure. J Biomech 1999;32(10):1037-47.

88. Ahmed A, Burke D, Yu A. In vitro measurement of static pressure distribution in synovial joints. II. Retropatellar surface. J Biomech Eng 1983;105:226-36.

89. Ateshian GA, Kwak SD, Soslowsky LJ, Mow VC. A stereophotogrammetric method for determining in situ contact areas in diarthrodial joints, and a comparison with other methods. J Biomech 1994;27(1):111-24.

90. Ateshian GA, Lai WM, Zhu WB, Mow VC. An asymptotic solution for the contact of two biphasic cartilage layers. J Biomech 1994;27:1347-60.

91. Guilak F, Mow V. The mechanical environment of the chondrocyte: a biphasic finite element model of cell matrix interactions in articular cartilage. J Biomech 2000;33:1663–73.

92. Mow V, Bachrach N, Setton L, Guilak F. Stress, strain, pressure, and flow fields in articular cartilage and chondrocytes. In: Mow V, Guilak F, Tran-Son-Tay R, Hochmuth R, eds. Cell Mechanics and Cellular Engineering. New York: Springer-Verlag; 1994:147-71.

93. Wu JZ, Herzog W. Finite element simulation of location- and time-dependent mechanical behavior of chondrocytes in unconfined compression tests. Ann Biomed Eng 2000;28(3):318-30.

94. Kwan MK, Lai WM, Mow VC. A finite deformation theory for cartilage and other soft hydrated connective tissues--I. equilibrium results. J Biomech 1990;23:145-55.

95. Hodge W, Fijan R, Carlson K, Burgess R, Harris W, Mann R. Contact pressures in the human hip joint measured in vivo. Proc Natl Acad Sci USA 1986;83:2879-83.

96. Soltz MA, Ateshian GA. Interstitial fluid pressurization during confined compression cyclical loading of articular cartilage. Ann Biomed Eng 2000;28(2):150-9.

97. Eberhardt AW, Keer LM, Lewis JL, Vithoontien V. An analytical model of joint contact. J Biomech Eng 1990;112:407-13.

98. Gu W, Mao X, Rawlins B, et al. Streaming potential of human lumbar annulus fibrosus is anisotropic and affected by disc degeneration. J Biomech 1999;32:1177-82.

99. Gu WY, Lai WM, Mow VC. Transport of fluid and ions through a porous-permeable charged-hydrated tissue, and streaming potential data on normal bovine articular cartilage. J Biomech 1993;26:709-23.

100. Gu WY, Lai WM, Mow VC. A mixture theory for charged-hydrated soft tissues containing multi-electrolytes: passive transport and swelling behaviors. J Biomech Eng 1998;120(2):169-80.

101. Frank EH, Grodzinsky AJ. Cartilage electromechanics-II. A continuum model of cartilage electrokinetics and correlation with experiments. J Biomech 1987;20:629-39.

102. Kim YJ, Bonassar LJ, Grodzinsky AJ. The role of cartilage streaming potential, fluid flow and pressure in the stimulation of chondrocyte biosynthesis during dynamic compression. J Biomech 1995;28:1055-66.

103. Chen AC, Bae WC, Schinagl RM, Sah RL. Depth- and strain-dependent mechanical and electromechanical properties of full-thickness bovine articular cartilage in confined compression. J Biomech 2001;34:1-12.

104. Chen AC, Nguyen TT, Sah RL. Streaming potentials during the confined compression creep test of normal and proteoglycan-depleted cartilage. Ann Biomed Eng 1997;25:269-77.

105. Huyghe J, Janssen J. Quadriphasic mechanics of swelling incompressible porous media. Int J Eng Sci 1997;35:793-802.

106. Frijns A, Huyghe J, Janssen J. A validation of the quadriphaisc mixture theory for intervertebral disc tissue. Int J Eng Sci 1997;35:1419-29.

107. Sun D, Gu W, Guo X, Lai W, Mow V. A mixed finite element formulation of triphasic mechano-electrochemical theory for charged, hydrated biological soft tissues. Int J Num Methods Eng 1999;45:1375-402.

108. Grodzinsky AJ, Lipshitz H, Glimcher MJ. Electromechanical properties of articular cartilage during compression and stress-relaxation. Nature 1978;275:448-50.

109. Basser PJ, Grodzinsky AJ. The Donnan model derived from microstructure. Biophys Chem 1993;46:57-68.

110. Buschmann MD, Grodzinsky AJ. A molecular model of proteoglycan-associated electrostatic forces in cartilage mechanics. J Biomech Eng 1995;117:179-92.

111. Lai WM, Mow VC, Sun DD, Ateshian GA. On the electric potentials inside a charged soft hydrated biological tissue: streaming potential versus diffusion potential. J Biomech Eng 2000;122:336-46.

112. Maroudas A, Wachtel E, Grushko G, Katz EP, Weinberg P. The effect of osmotic and mechanical pressures on water partitioning in articular cartilage. Biochim Biophys Acta 1991;1073:285-94.

113. Donnan F. The theory of membrane equilibria. Chem Rev 1924;1:73-90.

114. Maroudas A. Balance between swelling pressure and collagen tension in normal and degenerate cartilage. Nature 1976;260:808-9.

115. Maroudas A, Venn M. Chemical composition and swelling of normal and osteoarthrotic femoral head cartilage. II. Swelling. Ann Rheum Dis 1977;36(5):399-406.

116. LeRoux MA, Arokoski J, Vail TP, et al. Simultaneous changes in the mechanical properties, quantitative collagen organization, and proteoglycan concentration of articular cartilage following canine meniscectomy. J Orthop Res 2000;18:383-92.

117. Maroudas A, Ziv I, Weisman N, Venn M. Studies of hydration and swelling pressure in normal and osteoarthritic cartilage. Biorheology 1985;22:159-69.

118. Myers ER, Lai WM, Mow VC. A continuum theory and an experiment for the ion-induced swelling behavior of articular cartilage. J Biomech Eng 1984;106:151-8.

119. Grodzinsky AJ, Roth V, Myers E, Grossman WD, Mow VC. The significance of electromechanical and osmotic forces in the nonequilibrium swelling behavior of articular cartilage in tension. J Biomech Eng 1981;103:221-31.

120. Curnier A, He QC, Zysset P. Conewise linear elastic materials. J Elasticity 1995;37:1-38.

121. Soltz MA, Ateshian GA. A conewise linear elasticity mixture model for the analysis of tension-compression nonlinearity in articular cartilage. J Biomech Eng 2000;122:576-86.

122. Ehlers W, Markert B. A linear viscoelastic biphasic model for soft tissues based on the theory of porous media. J Biomech Eng 2001;123:418-24.

123. Ateshian GA, Warden WH, Kim JJ, Grelsamer RP, Mow VC. Finite deformation biphasic material properties of bovine articular cartilage from confined compression experiments. J Biomech 1997;30:1157-64.

124. Kwan MK, Hacker SA, Woo SL-Y, Wayne JS. The effect of storage on the biomechanical behavior of articular cartilage-a large strain study. J Biomech Eng 1992;114:149-53.

125. Lai W, Sun D, Ateshian G, Guo X, Mow V. Effects of inhomogeneous fixed charge density on the electrical signals for chondrocytes in cartilage. Proc ASME Symp Mechanics 2000;46:201–13.

126. Holmes MH, Mow VC. The nonlinear characteristics of soft gels and hydrated connective tissues in ultrafiltration. J Biomech 1990;23(11):1145-56.

127. Spilker RL, Suh J-K, Mow VC. Effects of friction on the unconfined compressive response of articular cartilage: a finite element analysis. J Biomech Eng 1990;112:138-46.

128. Suh J, Spilker R, Holmes M. A penalty finite element analysis for nonlinear mechanics of biphasic hydrated soft tissue under large deformation. Int J Num Methods Eng 1991;32:1411-39.

129. Spilker RL, Suh J-K, Mow VC. A finite element analysis of the indentation stress-relaxation response of linear biphasic articular cartilage. J Biomech Eng 1992;114:191-201.

130. Suh JK, Bai S. Finite element formulation of biphasic poroviscoelastic model for articular cartilage. J Biomech Eng 1998;120:195-201.

131. Wu JZ, Herzog W, Epstein M. Evaluation of the finite element software ABAQUS for biomechanical modelling of biphasic tissues. J Biomech 1998;31(2):165-9.

132. Cohen B, Lai WM, Mow VC. A transversely isotropic biphasic model for unconfined compression of growth plate and chondroepiphysis. J Biomech Eng 1998;120:491-96.

133. Wang C-B, Guo X, Deng J, Mow V, Ateshian G, Hung C. A novel noninvasive technique for determining distribution of fixed charge density within articular cartilage. In: Trans Orthop Res; 2001; 2001. p. 129.

134. Maroudas A. Transport of solutes through cartilage: permeability to large molecules. J Anat 1976;122:335-47.

135. Lai WM, Mow VC, Roth V. Effects of nonlinear strain-dependent permeability and rate of compression on the stress behavior of articular cartilage. J Biomech Eng 1981;103:61-6.

136. Chen SS, Falcovitz YH, Schneiderman R, Maroudas A, Sah RL. Depth-dependent compressive properties of normal aged human femoral head articular cartilage: relationship to fixed charge density. Osteoarthritis Cartilage 2001;9:561-9.

137. Valhmu WB, Stazzone EJ, Bachrach NM, et al. Load-controlled compression of articular cartilage induces a transient stimulation of aggrecan gene expression. Arch Biochem BIophys 1998;353:29-36.

138. Li LP, Shirazi-Adl A, Buschmann MD. Alterations in mechanical behaviour of articular cartilage due to changes in depth varying material properties--a nonhomogeneous poroelastic model study. Comput Methods Biomech Biomed Engin 2002;5(1):45-52.

139. Soulhat J, Buschmann MD, Shirazi-Adl A. A fibril-network-reinforced biphasic model of cartilage in unconfined compression. J Biomech Eng 1999;121:340-7.

140. Li LP, Buschmann MD, Shirazi-Adl A. A fibril reinforced nonhomogeneous poroelastic model for articular cartilage: inhomogeneous response in unconfined compression. J Biomech 2000;33(12):1533-41.

141. Li L, Soulhat J, Buschmann mD, Shirazi-Adl A. Nonlinear analysis of cartilage in unconfined ramp compression using a fibril reinforced poroelastic model. Clin Biomechanics 1999;14:673-82.

142. Huang CY, Stankiewicz A, Ateshian GA, Mow VC. Anisotropy, inhomogeneity, and tension-compression nonlinearity of human glenohumeral cartilage in finite deformation. J Biomech 2005;38(4):799-809.

143. Wang CC, Chahine NO, Hung CT, Ateshian GA. Optical determination of anisotropic material properties of bovine articular cartilage in compression. J Biomech 2003;36(3):339-53.

144. Mak AF. The apparent viscoelastic behavior of articular cartilage-the contributions from the intrinsic matrix viscoelasticity and interstitial fluid flows. J Biomech Eng 1986;108:123-30.

145. Hayes WC, Bodine AJ. Flow-independent viscoelastic properties of articular cartilage matrix. J Biomech 1978;11:407-19.

146. Zhu W, Mow VC, Koob TJ, Eyre DR. Viscoelastic shear properties of articular cartilage and the effects of glycosidase treatment. J Orthop Res 1993;11:771-81.

147. Bullough P, Jagannath A. The morphology of the calcification front in articular cartilage. J Bone Joint Surg Br 1983;65:72-88.

148. Clark JM. The structure of vascular channels in the subchondral plate. J Anat 1990;171:105-15.

149. Clark JM, Huber JD. The structure of the human subchondral plate. J Bone Joint Surg Br 1990;72(5):866-73.

150. Green WJ, Martin G, Eanes E, Sokoloff L. Microradiographic study of the calcified layer of articular cartilage. Arch Pathol 1970;90:151-8.

151. Oegema TJ, Carpenter R, Hofmeister F, Thompson RJ. The interaction of the zone of calcified cartilage and subchondral bone in osteoarthritis. Microsc Res Tech 1997;37:324-32.

152. Mente PL, Lewis JL. Elastic modulus of calcified cartilage is an order of magnitude less than that of subchondral bone. J Orthop Res 1994;12:637-47.

153. Wong BL, Bae WC, Sah RL. Accelerated stress-relaxation of cartilage due to chondral defects and subchondral bone plate perforation. Trans Orthop Res Soc 2006;52:1497.

154. Maroudas A, Bullough P, Swanson SA, Freeman MA. The permeability of articular cartilage. J Bone Joint Surg Br 1968;50(1):166-77.

155. Strangeways TSP. Observations on the nutrition of articular cartilage. Br Med J 1920;1:661-3.

156. Greenwald AS, Haynes DW. A pathway for nutrients from the medullary cavity to the articular cartilage of the human femoral head. J Bone Joint Surg Br 1969;51(4):747-53.

157. Bashir A, Gray ML, Boutin R, Burstein D. In vivo imaging of GAG in articular cartilage using delayed Gd(DTPA)2- enhanced MRI. Radiology 1997;205:551-8.

158. Ayotte DC, Ito K, Tepic S. Direction-dependent resistance to flow in the endplate of the intervertebral disc: an ex vivo study. J Orthop Res 2001;19(6):1073-7.

159. Hjertquist SO, Lemperg R. Histological, autoradiographic and microchemical studies of spontaneously healing osteochondral articular defects in adult rabbits. Calcif Tiss Res 1971;8:54-72.

160. Richmond J, Gambardella P, Schelling S, McGinty J, Schwartz E. A canine model of osteoarthritis with histologic study of repair tissue following abrasion arthroplasty. In: Trans Orthop Res; 1985; 1985. p. 10.

CHAPTER 2

THE ROLES OF DEPTH VARYING MECHANICAL PROPERTIES AND PERMEABILITY OF THE DEEP BOUNDARY CONDITION IN CONFINED COMPRESSION OF ARTICULAR CARTILAGE - POROELASTIC MODEL RESULTS

2.1 Abstract

Articular cartilage has depth-varying composition and structure that are manifest as depth-varying biomechanical properties. In addition, the subchondral bone region has a hydraulic permeability which is markedly increased in osteoarthritis. Thus, the effects of the depth-varying properties of articular cartilage and of the permeability of the deep boundary on the biomechanical behavior of cartilage were determined for oscillatory confined compression using a poroelastic multi-layer model. An (**a**) homogeneous and a (**b**) inhomogeneous sample structure, using experimentally derived parameters from bovine tissue, were simulated in two confined compression testing setups, one with an (**I**) impermeable base and (**II**) a freely-permeable base at 15% offset. The model results demonstrate that the high modulus and low permeability of the deep layer of cartilage normally provide a sealing effect, such that fluid pressurization and dynamic stiffness are maintained much more similarly for conditions **Ib** and **IIb** (~22% lower in IIb) than for conditions **Ia** and **IIa** (~50% lower

in IIa), with these differences between **I** and **II** diminishing at lower frequencies for both sample structures. Strain and solid stress were more distributed throughout the sample depth and propagated deeper into the tissue from permeable boundary conditions in **Ia** and **IIa** than in **Ib** and **IIb**. In summary, the depth varying properties of the inhomogeneous sample and an impermeable deep boundary provide increased fluid pressurization capability that when combined have a cumulative effect, effectively shielding the tissue from large strain and stress levels.

2.2 Introduction

Articular cartilage plays a fundamental role in all synovial joints allowing smooth, near frictionless motion between apposing bones and distributing joint loads over the joint surface [1-3]. Remarkably, this tissue functions oftentimes throughout an individual's life with little to no wear or damage. However, changes in cartilage and bone material properties associated with degeneration and injury can cause progressive wear, deformity, pain, decreased motion and disability. The effects of these changes on overall cartilage biomechanics remain to be fully elucidated [4-13].

Articular cartilage consists of a fluid phase including electrolytes and a solid phase primarily consisting of collagen and proteoglycan [1, 5, 10, 14-18]. The orientation of collagen changes with depth from a more parallel orientation to the articular surface superficially to a perpendicular orientation in the deep zones. Proteoglycan concentration in cartilage, along with negative fixed charge density, increases in magnitude with depth from the articular surface and is inversely related to the water content which decreases from 85% by wet weight near the surface to 70% near subchondral bone [1, 19-23]. This depth varying composition and structure is manifest biomechanically by a 30-fold increase in compressive modulus from superficial to deep and a 10-fold decrease in fluid permeability with depth [24-27].

When compressed, the load applied to cartilage is supported by a combination of the fluid phase pressure and the solid phase elastic stress that is dictated by the composition and structure, and hence the mechanical properties, of cartilage. Biphasic cartilage tissue models have revealed that the depth varying properties of cartilage produces a distribution of stresses and strains within the tissue in response to loads with the majority of compression in a normally depth varying cartilage sample occurring in the soft permeable superficial zone while the deep stiff impermeable zone shows little to no compression [14, 26, 27]. The inhomogeneous stress-strain state of depth varying cartilage provides insight into the fundamentals of the structure-function relationship in healthy articular cartilage [28].

The role of the subchondral bone plate (ScBP) in the mechanical behavior of the overlying cartilage remains to be clarified, namely the fluid transport properties of the zone of calcified cartilage at the cartilage-bone junction. Subchondral bone plate changes have been documented in pathological conditions [13, 29-38]. Recent direct permeability measurements have shown an increase in permeability of osteochondral cores and the subchondral bone plate with progression of osteoarthritis [13]. An increase in permeability of cartilage combined with an increase in permeability of the subchondral bone plate could markedly decrease the ability of cartilage to maintain fluid pressure thus exposing the solid matrix to pathological stress-strain levels. For example, a penalty biphasic model showed that a freely permeable subchondral bone defect 1.5 mm wide allows cartilage to reach steady state faster in oscillatory compression. Strain was shown to be significantly larger when the subchondral bone plate is permeable than when the subchondral bone plate is impermeable [37]. Furthermore, a 2-D linear biphasic finite element analysis showed that with a perforation in the subchondral bone plate, solid matrix stresses and strains are significantly increased as a consequence of diminished fluid pressurization in the region of the defect [38].

The objective of this study was to determine the effects of depth varying mechanical properties of cartilage and the permeability of the deep boundary condition, representing the subchondral bone plate, on stiffness and the depth profiles for strain, solid stress and fluid pressure in oscillatory confined compression using a previously described poroelastic multilayer model by comparing the four combinations of two sample types, homogeneous (H) and inhomogeneous (I), and two deep boundary conditions, impermeable (I) and permeable (II) [39].

2.3 Methods

Nomenclature

Symbol	Units	Definition
$d1$	[]	material constant
δ, δ^{offset}, δ^i	[m]	sample thickness, offset sample thickness, of layer i
$\varepsilon_{z,}$, ε_z^i, ε, ε^i	[]	offset strain, offset strain in layer i, small superimposed axial strain, axial strain at interface i (complex number representing amplitude and phase)
f	[1/s]	frequency
γ, γ^i	[1/m]	1/skin depth, of layer i
H_A, H_{A0}, $H_A^{i,}$, H_{A0}^i	[Pa]	confined compression modulus of homogeneous model at a specified strain offset, at zero strain offset, of layer i in multilayer model at a specified strain offset, at zero strain offset
k_p, k_{p0}, k_p^i, k_{p0}^i	[m^2/Pa s]	open-circuit hydraulic permeability of homogeneous model at a specified strain offset, at zero strain offset, of layer i in multilayer model at a specified strain offset, at zero strain offset
M, M^i	[]	deformation dependence constant for permeability in homogeneous model, for layer i in multilayer model
n	[]	number of layers in multilayer model
σ^s, $\sigma^{s,0}$, $\sigma^{s,i}$, $\sigma^{s,n}$	[Pa]	axial solid stress, at top surface, at interface i, at the bottom (complex number representing amplitude and phase)

σ^T	[Pa]	total (axial) stress (complex number representing amplitude and phase)
P_f	[Pa]	fluid pressure (complex number representing amplitude and phase)
t	[s]	time
$u^0, u^i, u(z), u^n$	[m]	dynamic oscillatory displacement at the top, at layer interface i, as a function of z, at the bottom (complex number representing amplitude and phase)
U_z	[m/s]	area averaged axial fluid velocity (complex number representing amplitude and phase)
z	[m]	coordinate in axial direction

Subscripts and superscripts

(f)	reference to fluid phase
(i)	layer index
(s)	reference to solid phase

Testing setup references

I	confined compression testing setup I
II	confined compression testing setup II
H	homogeneous sample construct
INH	inhomogeneous sample construct
bd	displacement applied to bottom
td	displacement applied to top

I. Homogeneous Model

The linear analysis of the mechanics of small oscillations superimposed on a static offset compression, ε_z, applied to a homogeneous layer of tissue has been previously described [40]. The equilibrium (i.e., offset) stress-strain response has been described by

$$\sigma = \frac{H_{A0}}{4}\left[1 + d_1\varepsilon_z\right]\left[\frac{(1+\varepsilon_z)^4 - 1}{(1+\varepsilon_z)^3}\right] \quad (1)$$

where σ is the equilibrium stress, d_1 ranges from 0.7 to 0.9, H_{A0} is the equilibrium modulus for small strain, and ε_z is the equilibrium strain or offset [41]. When reduced to a single unknown parameter (H_{A0}) by assuming $d_1 = 0.9$, this expression has been found to provide a good fit of data from full-thickness articular cartilage [42] as well as layers within articular cartilage [26, 27].

The strain dependence of permeability has been described by [43]

$$k_p(\varepsilon_z) = k_{p0}e^{M\varepsilon_z} \quad (2)$$

where k_{p0} is the permeability at zero strain, and M is a parameter that describes the strain dependence.

For small superimposed strains, the linear, one dimensional constitutive equation is

$$\sigma^T(z,t) = H_A\varepsilon(z,t) - P_f(z,t) \quad (3)$$

where σ^T is the total axial stress, H_A the equilibrium confined compression modulus for a specific offset strain, ε, the small superimposed axial strain and P_f the interstitial fluid pressure [14, 44, 45]. In the absence of current (i.e., the open-circuit condition) and without imposed fluid flow, the fluid velocity and fluid pressure gradient are related by the hydraulic permeability,

$$U_z = -k_p \frac{\partial P_f(z,t)}{\partial z} \quad (4)$$

The H_A of Eqn. (3) can be calculated using the stress-strain relationship of Eqn. (1) for a particular H_{A0} and strain offset, ε_z, as the tangent modulus normalized to the compressed tissue thickness, i.e.,

$$H_A(\varepsilon_z) = \frac{\partial \sigma_z}{\partial \varepsilon_z}(1-\varepsilon_z) \quad (5)$$

Analogously, k_p of Eqn. (4) can be calculated from Eqn. (2) if k_{p0}, M, and ε_z are given.

Eqns. (3)-(5) have been solved under oscillatory steady-state conditions in which a dynamic oscillatory displacement, u^0, and frequency, f, is assumed at the top, free-draining cartilage surface, and zero amplitude is assumed at the bottom, impermeable surface. The resultant expression for dynamic oscillatory stress, σ^0 can be expressed as a function of $H_A(\varepsilon_z)$, $k_p(\varepsilon_z)$, d, and f [44].

II. Layered Model for Testing Setup I (Figure 2.1B, top)

The biomechanics of dynamic oscillatory compression has also been analyzed for cartilage that is modeled as a stack of individual homogeneous layers of tissue [39]. When subjected to an overall static compression offset, ε_z, with a superimposed oscillation, u^0, Eqns. (1)-(5) can be applied to each of the n (i = 1, 2,..., n) layers. For layers with different equilibrium stress-strain properties, i.e., different H_A^i, the resultant static offset stretch in each layer, ε_z^i, can be computed by applying Eqn. (1) to each layer, assuming that the equilibrium stress is the same in each layer, and setting the overall offset displacement equal to the sum of the offset displacements in each layer [26, 27].

The oscillatory small-strain analysis has been described previously [39]. There are n+1 (0, 1, 2, n) interfaces, with the ith layer bounded by a top interface (i-1) and a bottom interface (i). Using boundary conditions at each interface of continuous stress of the solid phase, $\sigma^{s,i}$, and displacement, u^i, and layers with material properties, H_A^i, k_p^i, δ^i, and γ^i,

$$\begin{bmatrix} \sigma^{s,0} \\ u^0 \end{bmatrix} = \prod_{i=1}^{n} \begin{bmatrix} \cosh \gamma^i \delta^i & H_A{}^i \gamma^i \sinh \gamma^i \delta^i \\ \sinh \gamma^i \delta^i / H_A{}^i \gamma^i & \cosh \gamma^i \delta^i \end{bmatrix} \begin{bmatrix} \sigma^{s,n} \\ u^n \end{bmatrix} \quad (6)$$

$\sigma^{s,0}$ and u^0 are the solid stress and displacement, respectively, at the top surface (z=0), and $\sigma^{s,n}$ and u^n are the solid stress and displacement, respectively, at the bottom of the test sample and γ^i has been defined as $\sqrt{j2\pi f / H_A{}^i k_p{}^i}$, representing 1/skin depth of mechanical penetration. In Eqn. (6), $\sigma^{s,n}$ or $\sigma^{s,0}$ can be eliminated by setting, respectively, the bottom or top displacement, u^n or u^0, to zero, to obtain a relationship between $\sigma^{s,0}$ and u^0 or $\sigma^{s,n}$ and u^n. At the displaced surface, P_f in Eqn. (3) is taken to be zero (freely permeable boundary condition), so that $\sigma^{s,0}$ or $\sigma^{s,n}$ is equivalent to the total stress, σ^T. With this approach, dynamic displacement, strain, solid stress and fluid pressure at each interface and within each layer can be calculated.

III. Layered Model for Testing Setup II (Figure 2.1B, bottom)

Setup II solutions were obtained by superimposing the linear solutions for displacement, strain and solid stress with the sample in a setup I (td) condition (sample displaced from the top with the bottom fixed in space) and in a setup I (bd) condition (sample displaced from the bottom with the top fixed in space) (Figure 2.2)

$$u(z)^{II} = u(z)^{td} + u(z)^{bd} \quad (7)$$

$$\varepsilon(z)^{II} = \varepsilon(z)^{td} + \varepsilon(z)^{bd} \quad (8)$$

$$\sigma(z)^{s,II} = \sigma(z)^{s,td} + \sigma(z)^{s,bd} \quad (9)$$

Fluid pressure is the total stress (ie - the top or bottom surface stress) minus the solid stress

$$P_f(z) = \sigma^{s,0,II} - \sigma^{s,II}(z) \quad (10)$$

The fluid pressure at the top and bottom of setup II was zero by definition for the freely permeable boundary conditions leaving the solid stresses at the top and bottom of the sample equal to satisfy Eqn. (3)

$$\sigma^{s,0,td} + \sigma^{s,n,bd} = \sigma^{s,n,td} + \sigma^{s,o,bd} \quad (11)$$

The expressions for the individual surface stress terms at the top, $\sigma^{s,0,td}$ and $\sigma^{s,n,bd}$, and bottom, $\sigma^{s,n,td}$ and $\sigma^{s,0,bd}$, can be obtained from Eqn. (6) by applying the individual displacement amplitudes, $u^{0,td}$ and $u^{0,bd}$, for setup I (td) and setup I (bd) respectively, which can be calculated from

$$u^{0,td} - u^{0,bd} = u^{0,II} \quad (12)$$

where $u^{0,II}$ is the desired dynamic displacement in setup II.

Stiffness was calculated by dividing the surface solid stress, $\sigma^{s,0,II}$, by the dynamic strain amplitude (u^0/δ^{offset}).

For an inhomogeneous sample at offset equilibrium, the solid stress throughout a multi layer model is constant and a bulk equilibrium compressive moduli at a specific offset can be determined by a weighted average as

$$H_{Aeq,offset-strain} = \frac{\delta_{total}}{\sum_{i=1}^{n} \frac{\delta_i}{H_{Ai}}} \quad (13)$$

All simulations were performed on a PC with MATLAB software (The Mathworks Inc., Natick, MA) and a Multiple Precision Toolbox (Ben Barrowes, 2004) for increased numerical precision. Sample parameters were taken from a previous study using bovine tissue (Figure 2.1A)[40]. Frequency range was 0.00001 – 1 Hz. Dynamic displacement amplitude, $|u^0|$, was 0.1% of offset thickness. Strain amplitudes were normalized to 0.1% strain. Solid stress and fluid pressure were normalized to solid stress amplitude.

2.4 Results

Both the setup and tissue homogeneity affected dynamic stiffness with an interactive effect, with phase affected at low frequencies (dashed lines, Figure 2.3) and amplitude at high frequencies (solid lines, Figure 2.3). With setup I, dynamic stiffness was fairly similar for both sample types throughout the frequency range. With the permeable base of setup II, the phase angle was reduced for both samples and the stiffness amplitude was reduced, in the homogeneous model by 50%, but only by 22% in the inhomogeneous model. The dynamic stiffness in setup II for INH was 60% greater than H for frequencies above 0.004 Hz.

At low frequency (i.e. 0.0001 Hz), strain, stress, and fluid pressure (Figure 2.4A-C) exhibited depth-associated variation consistent with the test setup and tissue composition. Strain, shown as normalized amplitude (Figure 2.4A), was continuous near 1.0 with depth for the homogeneous sample and was discontinuous for the inhomogeneous sample due to the discontinuity in compressive moduli at layer interfaces, highest in the superficial zone and decreased with depth in a stepwise fashion with layer. Comparing setup II relative to I, normalized solid stresses (Figure 2.4B) at the top surface was lower by 5.6% for the homogeneous and 15.6% for the inhomogeneous sample and at the base, normalized solid stress was lower by 13% for the inhomogeneous sample. Comparing setup II relative to I, fluid pressure (Figure 2.4C) increased with depth in both setups but in setup II then decreased to zero at the base. Fluid pressure at the base in setup I was 160% larger for the inhomogeneous sample than for the homogeneous sample.

At higher frequencies (Figures 2.4D-F and 2.5A-F), comparing setup II relative to I, strain at the top surface was lower by 50% for the homogeneous and 23% for the inhomogeneous sample (Figures 2.4D and 2.5A). Within setup, strain at the top surface and at the base for the inhomogeneous sample was larger than the homogeneous sample but these levels diminished quickly towards zero for the inhomogeneous sample while the homogeneous sample had larger strains penetrate deeper in the tissue (Figures 2.4D and 2.5AD). The stress at the top surface for both samples in setup I were similar (Figures 2.4E and 2.5B). Comparing setup II relative to I, normalized solid stresses at the top surface was lower by 50% for the homogeneous and 22% for the inhomogeneous sample (Figures 2.4E and 2.5B). Within setup, stress at the top surface and at the base for the inhomogeneous sample was larger than the homogeneous sample but these levels diminished quickly towards zero for the inhomogeneous sample while the homogeneous sample had larger stresses penetrate deeper in the tissue (Figures 2.4E and 2.5BE). Comparing setup II relative to I, fluid pressure increased with depth then plateaus in both setups but in setup II then decreased to zero at the base with the fluid pressure plateaus lower by 50% for the homogeneous and 22% for the inhomogeneous sample (Figures 2.4F and 2.5CF).

Phase angles were continuous for all four conditions with the number of cycles of phase rising with frequency for strain and solid stress phase angles which were the same (Figure 2.6A-F). At 0.01 and 1 Hz, H and INH in II had phase angles for strain, solid stress and fluid pressure that were symmetric about mid-depth and 60% depth from the top, respectively, and were similar to H and INH in I for the top 45% and 55% of depth, respectively, for strain and solid stress and for much more of the depth for fluid pressure. Increasing frequency also increased the localization of fluid pressure phase angle variability nearer permeable boundaries with a constant phase angle through most of the sample (Figure 2.6D-F).

2.5 Discussion

Articular cartilage has depth-varying composition and structure that are commonly represented by depth-varying biomechanical properties of experimentally derived compressive modulus and hydraulic permeability [24-28]. The subchondral support of articular cartilage has a hydraulic permeability that is increased with osteoarthritis, and the difference between the normally sealing basal boundary and the abnormally permeable boundary, can be modeled as two extremes with a normal-like impermeable base or an osteoarthritis-like permeable base [13, 29-38]. The influence of these depth-varying properties and setups on the bulk tissue stiffness and depth profiles of strain, solid stress and fluid pressure were analyzed with a previously developed multi-layer poroelastic model, assuming a physiological test protocol of 15% offset compression, with 0.1% oscillation superimposed at frequencies up to 1 Hz [39].

Figures 2.4 and 2.5 illustrate the fundamental roles of tissue inhomogeneity, with the superficial region being soft and permeable, and the deep region being stiff and relatively impermeable resulting in relatively higher compressive strain magnitude in the superficial layer (coincident with larger fluid exudation), and relatively little compression in (and little fluid exudation from) the deep layer. The high modulus and low permeability of the deep layer of cartilage provides a sealing effect, such that fluid pressurization and dynamic stiffness are maintained much more similarly for the inhomogeneous sample in setups I and II than for the homogeneous sample. The depth varying properties of the inhomogeneous sample as well as an impermeable deep test boundary facilitate fluid pressurization that effectively shields cartilage from excessive strain and stress levels.

A novelty of this study was the modeling of confined compression setup II using superposition of the linear biphasic poroelastic model (Figure 2.2). Setup II generally had a dampening effect on stiffness and the strain, solid stress and fluid pressure near the surface while introducing higher levels of strain and solid stress near the base as fluid is exuded from both the top and bottom in this setup (Figures 2.4 and 2.5). The homogeneous sample in setup II is symmetric at half depth as expected (Figures 2.4 and 2.5). The fluid pressure depth profiles (Figures 2.4CF and 2.5CF) indicate that the majority of stiffness is attributed to fluid pressurization as opposed to solid stress elasticity which reduces to zero throughout much of the sample (Figures 2.4BE and 2.5BE). This allows cartilage to support large loads with relatively low compressive moduli. At 1 Hz, I-H stiffness was 48 MPa with a tissue compressive moduli of only 0.513 MPa (Figure 2.3). The stiffness of II-H at 1 Hz was 24 MPa, 50% less than I-H, with the same tissue parameters and dimensions as in I-H, with II-H having 50% less fluid pressure than in I-H (Figures 2.3 and 2.5CF). This is also seen in INH, but to a lesser degree, with II-INH 22% less stiff than I-INH with correspondingly 22% less fluid pressure (Figures 2.3-2.5).

The ability of II-INH to maintain more fluid pressure than II-H can be attributed to layer 3, or the deep layer, of INH, which is 81% less permeable and 56% stiffer than layer 1. This layer effectively functions as a stiff hydraulic seal at the bottom of the sample, enabling II-INH to preserve much of the stiffness of I-INH by preferentially guiding fluid exudation thru the top moreso than the bottom. Although the fluid pressure gradient is larger near the bottom of II-INH than of II-H (Figures 2.4F and 2.5I), the fluid flow and velocity, per Eqn. (4), is larger through the bottom of II-H than of II-INH because of the increased depth of penetrance of large strains and the nearly nine-fold higher permeability of II-H than II-INH in this region. Furthermore, the large strains at the top and bottom of INH compared to H (Figures 2.4AD and 2.5A-C) serve to further pressurize interstitial fluid by compressing the solid pores in this region, decreasing permeability as dictated by Eqn. (2) and essentially trapping fluid beneath this zone [1, 6, 14-18, 46-52]. It is interesting to note at 0.01 and 1 Hz, the fluid pressure can exceed the applied solid stress at the top. This occurs where strain is tensile relative to the applied strain offset while the total solid stress is compressive and vice versa, i.e., when cyclical deformation lags the total stress.

The stiffness parameters used in this study were obtained using theoretical models to estimate modulus and permeability from experimentally derived data from confined compression testing of normal cartilage from adult bovine patellofemoral groove [40]. The depth dependence of these properties was assessed by performing tests on full- and partial-thickness specimens and fitting the data to a three-layer as well as a homogeneous model as described above. The strain dependence of these properties was analyzed by fitting static and dynamic experimental data, obtained at various levels of static compression with superimposed low-amplitude oscillations to the theory. Although this study attempts to simulate an osteoarthritic subchondral bone plate by using a freely permeable boundary condition, the stiffness parameters used in these simulations are from normal cartilage. With degeneration, cartilage thins and becomes more permeable. The homogeneous sample in this study is more permeable and could roughly represent an osteoarthritic cartilage sample as the permeability of the homogeneous sample is nearly 10 times that of the deep layer of the inhomogeneous sample. The results presented in this study also highlight the importance of the depth varying properties of cartilage.

The observed depth- and strain-dependence in the properties of cartilage suggests that the test protocol and method of data analysis will affect the resultant estimates of the material properties. The choice of oscillation frequencies is likely to have an effect because the model predicts that strain penetration exhibits a characteristic distance, $1/\gamma$ ($=\sqrt{H_A{}^i k_p{}^i/j2\pi j}$), that is dependent on frequency. Thus, data acquired at relatively high frequencies would be strongly influenced by the properties of the material closely situated under the test platen, whereas data at low frequencies would be influenced relatively more by tissue properties somewhat further into the tissue. In that regard, the importance of the number of layers (and their corresponding gradient of mechanical properties) used in these simulations becomes important.

The superficial layer used in these simulations represents the top 28.5% of the depth of the sample. At low frequency, the strain penetrance exceeds the depth of the first layer (Figure 2.4). At high frequency, the strain penetrance is less than 6% of the depth of the sample (Figure 2.5). Increasing the number of layers in the region of strain penetrance, both at the superficial and deep portions of the sample in setup II but only at the superficial surface in setup I, would increase the accuracy of the simulations but increasing the number of layers in the region where strain is zero or near zero would likely have little to no effect on the simulations performed in this study. However, experimentally deriving mechanical data for the top 6% of the depth of the sample in the case of high frequency simulations may be impossible and would likely have to be derived theoretically or interpolated.

The low permeability of cartilage allows it to support large loads through interstitial fluid pressurization to maintain prolonged load support and minimize solid matrix strain and stress [53]. The duration of this load support by fluid pressurization to reach equilibrium is characterized by a viscoelastic time constant, τ (= $h^2/H_A k$), which is dependent on the tissue thickness, h, permeability, k, and compressive modulus, H_A [54]. With increased hydraulic conductance of both articular cartilage and the subchondral bone plate, an increase of fluid exudation through the subchondral bone plate will lead to shorter equilibrium times and large deformations that can accelerate solid matrix degeneration. These means provide a mechanical mechanism for the progression of osteoarthritis that includes both degenerative changes in cartilage depth varying properties, from an inhomogeneous to a relatively more homogeneous construct and accompanying degenerative changes in the permeability of the subchondral bone plate that together may substantially impair the ability of cartilage to pressurize interstitial fluid and thus stiffness. In addition, pathological strain and stress levels may alter the biomechanical milieu of chondrocytes providing for a cellular mechanism for the progression of osteoarthritis.

2.6 Acknowledgments

This chapter, in full, will be submitted to the *Journal of Biomechanics.* The thesis author is the primary author and thanks co-authors, Drs. Albert Chen and Robert Sah. This work was supported by two NIH short term training grants, T35 HL00749-25 and T32 HL007087-31 (for JJL) and NIH R01 AR044058, NIH R01 AR051565, and the Howard Hughes Medical Institute Professor's Award to UCSD (for RLS).

2.7 Figures

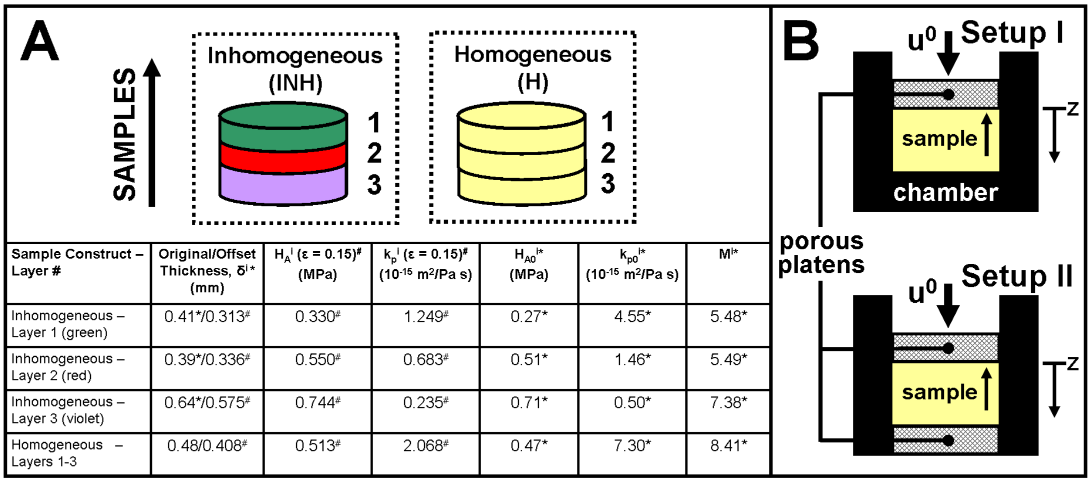

Sample Construct – Layer #	Original/Offset Thickness, δ^{i}* (mm)	H_A^i (ε = 0.15)# (MPa)	k_p^i (ε = 0.15)# (10^{-15} m^2/Pa s)	H_{A0}^{i*} (MPa)	k_{p0}^{i*} (10^{-15} m^2/Pa s)	M^{i*}
Inhomogeneous – Layer 1 (green)	0.41*/0.313#	0.330#	1.249#	0.27*	4.55*	5.48*
Inhomogeneous – Layer 2 (red)	0.39*/0.336#	0.550#	0.683#	0.51*	1.46*	5.49*
Inhomogeneous – Layer 3 (violet)	0.64*/0.575#	0.744#	0.235#	0.71*	0.50*	7.38*
Homogeneous – Layers 1-3	0.48/0.408#	0.513#	2.068#	0.47*	7.30*	8.41*

Figure 2.1 Sample Types and Confined Compression Testing Setups. (**A**) Inhomogeneous, INH, and homogeneous, H, sample types, arrow pointing to sample surface, with tissue parameters (*: H_{A0}^{i}, k_{p0}^{i}, M^{i} and δ^{i} taken from Chen, 2001; # 15% offset values obtained using finite deformation theory of cartilage, Eqn. (5), and strain dependent permeability, Eqn. (2)). (**B**) Confined compression testing setup I (1 permeable boundary condition) and II (2 permeable boundary conditions). Depth, *z*, was measured from the top surface where dynamic displacement, u^0, was applied. No displacement condition ($u = 0$) at the bottom of sample.

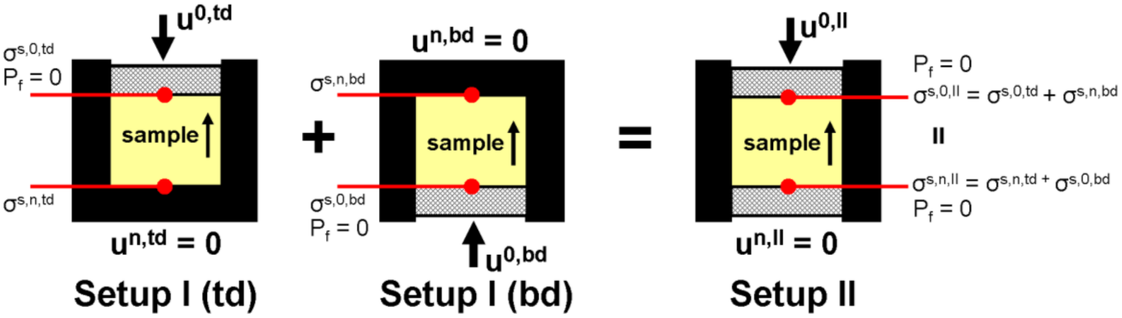

Figure 2.2 Confined Compression Testing Setup II. Setup II results were obtained by superimposing the linear solutions for the sample in two individual conditions, left and middle (td and bd), which together combine to create the boundary conditions defined by setup II, right. $u^{0,td}$, $u^{0,bd}$: dynamic displacement applied to the top or bottom. $u^{n,td}$, $u^{n,bd}$: displacement at the bottom or top with displacement applied to the top or bottom. $\sigma^{s,0,td}$: solid stress on top with dynamic displacement applied to top; $\sigma^{s,n,td}$: solid stress on bottom with dynamic displacement applied to top; $\sigma^{s,0,bd}$: solid stress on bottom with dynamic displacement applied to bottom; $\sigma^{s,n,bd}$: solid stress on top with dynamic displacement applied to bottom; $\sigma^{s,0,II}$: solid stress on top in setup II; $\sigma^{s,n,II}$: solid stress on bottom in setup II. P_f: fluid pressure. ε: strain.

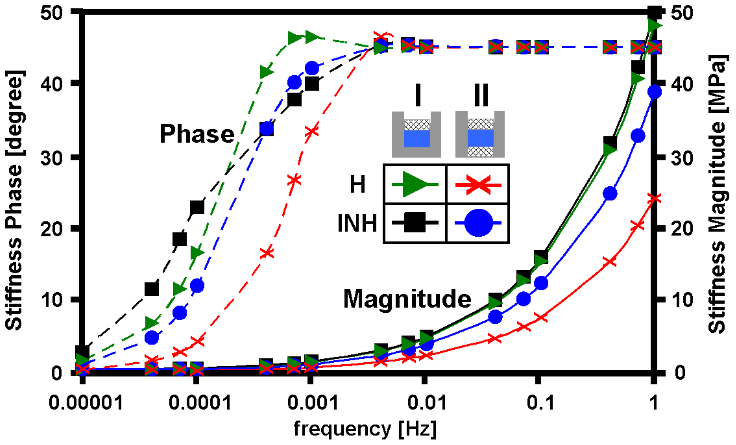

Figure 2.3 Dynamic Stiffness Magnitude (solid lines [MPa]) and Phase (dashed lines [degree]) at 0.1% dynamic displacement of offset thickness for inhomogeneous, INH, and homogeneous, H, sample types in confined compression setup I and II, frequency range 0.00001-1 Hz. Sample parameters as defined in Figure 2.1.

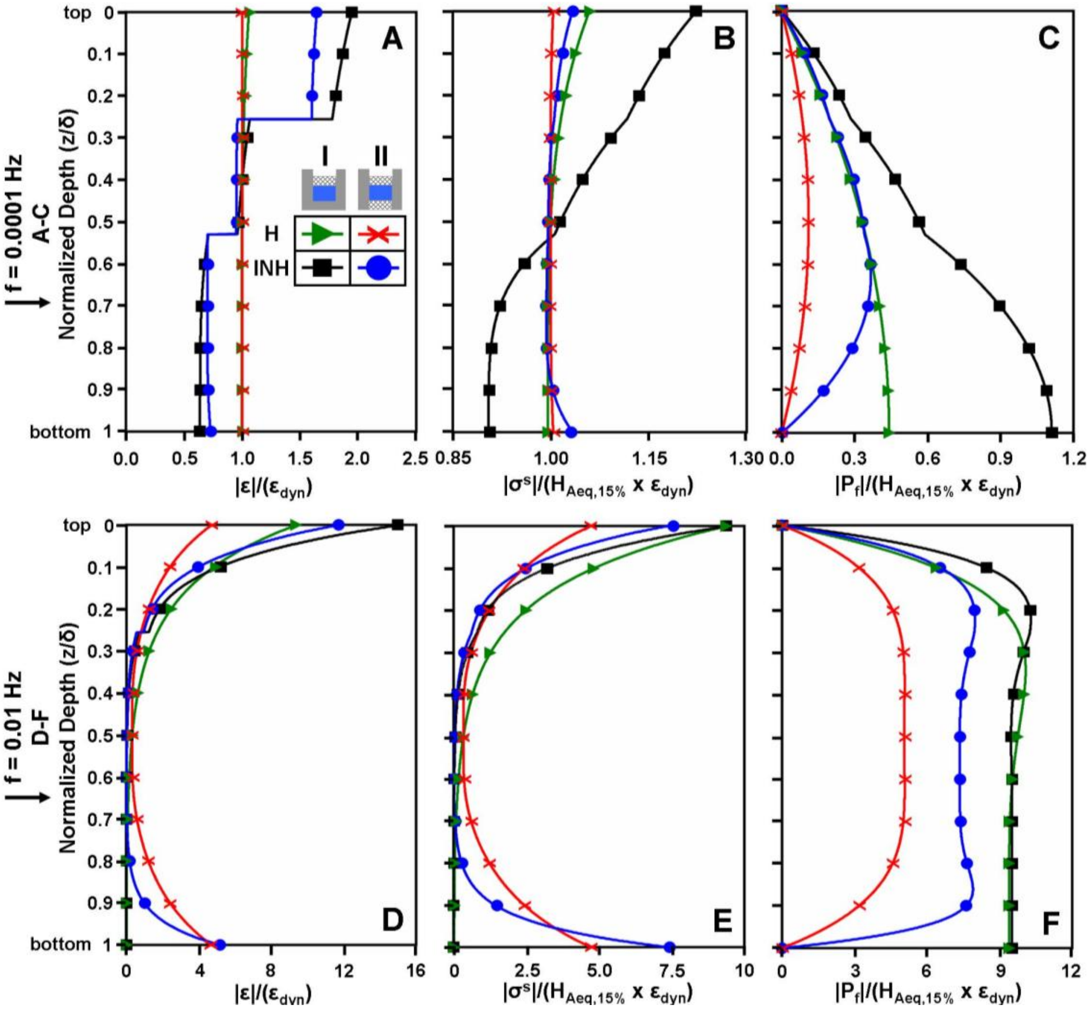

Figure 2.4 Strain, $|\varepsilon|$, Solid Stress, $|\sigma^s|$, and Fluid Pressure, $|P_f|$, Amplitudes for low (0.0001 Hz) and intermediate (0.01 Hz) frequencies for homogeneous, H, (green arrowhead and red x) and inhomogeneous, INH, (black box and blue circle) sample types in I (green arrowhead and black box) and II (red x and blue circle). **(A)** and **(D)** Strain amplitudes for low (0.0001 Hz) and intermediate (0.01 Hz) frequency normalized to 0.1% dynamic strain, ε_{dyn}. **(B)** and **(E)** Solid stress amplitudes normalized to dynamic stress amplitude, or $H_{Aeq,}$ x $\varepsilon_{dyn.}$ **(C)** and **(F)** Fluid pressure amplitudes normalized to dynamic stress amplitude, or H_{Aeq} x ε_{dyn}. 15% offset compression. Dynamic strain amplitude, $|\varepsilon_{dyn}|$, 0.1% of offset thickness. H_{Aeq} from Eqn. (13).

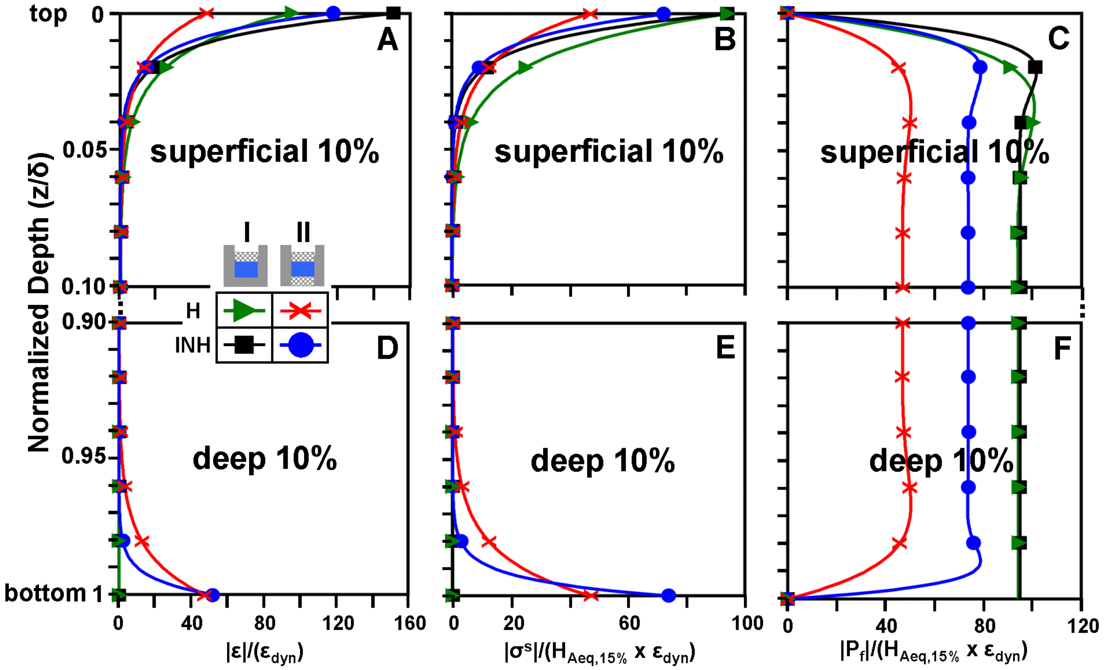

Figure 2.5 Strain, $|\varepsilon|$, Solid Stress, $|\sigma^S|$, and Fluid Pressure, $|P_f|$, Amplitudes for high frequency (1 Hz) for homogeneous, H, (green arrowhead and red x) and inhomogeneous, INH, (black box and blue circle) sample types in I (green arrowhead and black box) and II (red x and blue circle) with magnification of the superficial 10% **(A-C)** and deep 10% of sample depth **(D-F)**. **(A)** and **(D)** Strain amplitudes normalized to 0.1% dynamic strain, ε_{dyn}. **(B)** and **(E)** Solid stress amplitudes normalized to dynamic stress amplitude, or H_{Aeq} x ε_{dyn}. **(C)** and **(F)** Fluid pressure amplitudes normalized to dynamic stress amplitude, or H_{Aeq} x ε_{dyn}. 15% offset compression. Dynamic strain amplitude, $|\varepsilon_{dyn}|$, 0.1% of offset thickness. H_{Aeq} from Eqn. (13).

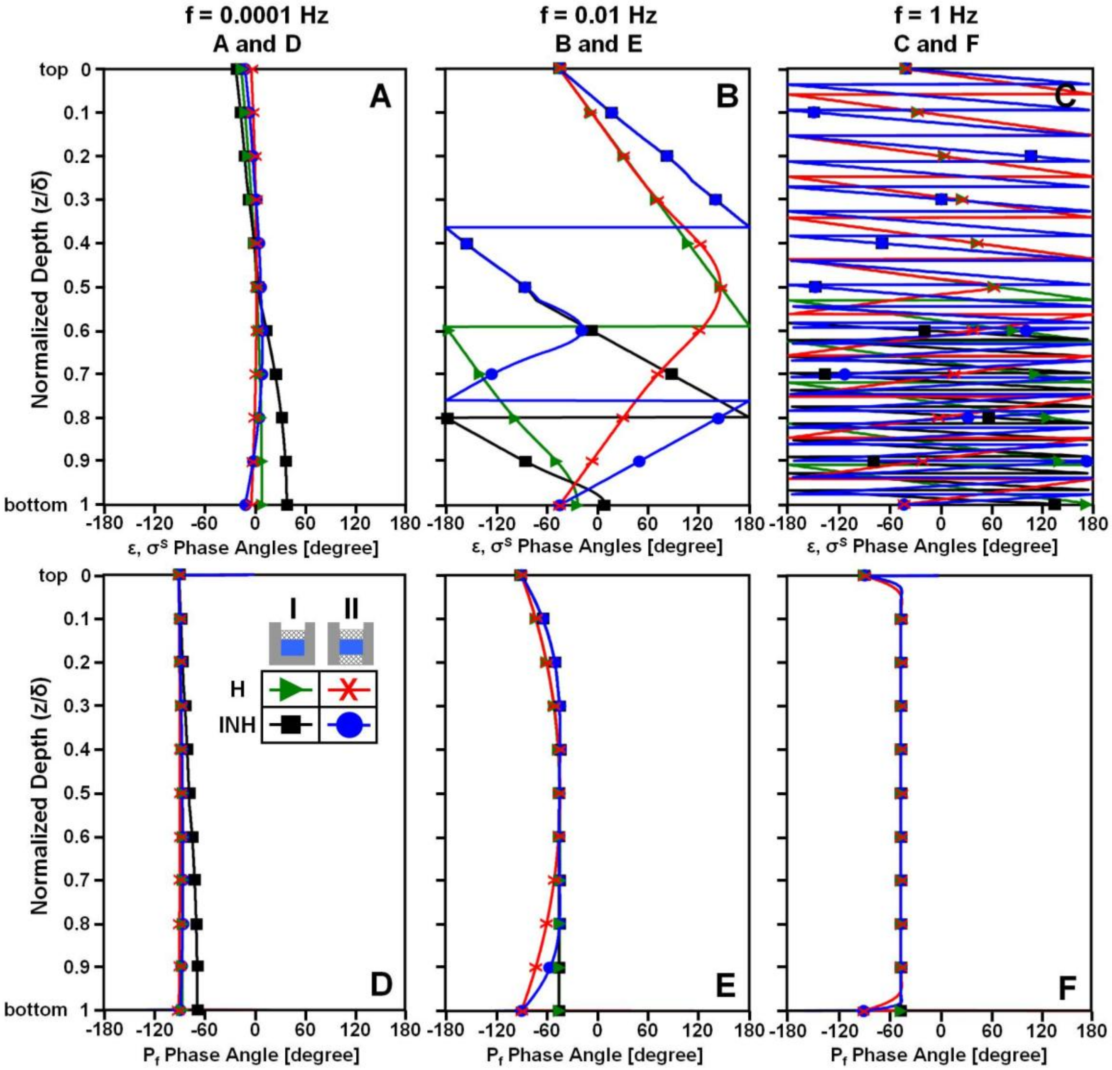

Figure 2.6 Strain, ε, Solid Stress, σ^s, and Fluid Pressure, P_f, Phase for low (0.0001 Hz, **AD**), intermediate (0.01 Hz, **BE**) and high (1 Hz, **CF**) frequencies for homogeneous, H, and inhomogeneous, INH, sample types in I and II. **(A-C)** Strain and solid stress phase angles. **(D-F)** Fluid pressure phase angles. Phase angles for solid stress and strain are equivalent. 15% offset compression. Dynamic strain amplitude, $|\varepsilon_{dyn}|$, 0.1% of offset thickness.

2.8 References

1. Mow VC, Ratcliffe A. Structure and function of articular cartilage and meniscus. In: Mow VC, Hayes WC, eds. Basic Orthopaedic Biomechanics. 2nd ed. New York: Raven Press; 1997:113-78.

2. Mow VC, Ateshian GA, Spilker RL. Bioemechanics of diarthodial joints: a review of twenty years of progress. J Biomech Eng 1993;115:460-7.

3. Mow VC, Ateshian GA. Lubrication and wear of diarthrodial joints. In: Mow VC, Hayes WC, eds. Basic Orthopaedic Biomechanics. 2nd ed. New York: Raven Press; 1997:275-315.

4. Akizuki S, Mow VC, Muller F, Pita JC, Howell DS, Manicourt DH. Tensile properties of human knee joint cartilage: II. correlations between weight bearing and tissue pathology and the kinetics of swelling. J Orthop Res 1987;5:173-86.

5. Armstrong CG, Mow VC. Variations in the intrinsic mechanical properties of human articular cartilage with age, degeneration, and water content. J Bone Joint Surg Am 1982;64-A:88-94.

6. Maroudas A. Physico-chemical properties of articular cartilage. In: Freeman MAR, ed. Adult Articular Cartilage. 2nd. ed. Tunbridge Wells, England: Pitman Medical; 1979:215-90.

7. Mankin HJ, Mow VC, Buckwalter JA. Articular cartilage repair and osteoarthritis. In: Am Acad Orthop Surg; 2000; Rosemont, IL; 2000.

8. Eyre DR, Dickson IR, van Ness K. The collagens of articular cartilage. Sem Arthritis Rheum 1991;21,S2:2-11.

9. Clark JM, Simonian PT. Scanning electron microscopy of "fibrillated" and "malacic" human articular cartilage: technical considerations. Microsc Res Tech 1997;37:299-313.

10. Setton LA, Zhu W, Mow VC. The biphasic poroviscoelastic behavior of articular cartilage: role of the surface zone in governing the compressive behavior. J Biomech 1993;26:581-92.

11. Guilak F, Ratcliffe A, Lane N, Rosenwasser MP, Mow VC. Mechanical and biochemical changes in the superficial zone of articular cartilage in canine experimental osteoarthritis. J Orthop Res 1994;12:474-84.

12. Jeffrey JE, Thomson LA, Aspden RM. Matrix loss and synthesis following a single impact load on articular cartilage in vitro. Biochim Biophys Acta 1997;1334:223-32.

13. Hwang J, Bae WC, Shieu W, Lewis CW, Bugbee WD, Sah RL. Increased hydraulic conductance of human articular cartilage and subchondral bone plate with progression of osteoarthritis. Arthritis Rheum 2008;58:3831-42.

14. Mow VC, Kuei SC, Lai WM, Armstrong CG. Biphasic creep and stress relaxation of articular cartilage in compression: theory and experiment. J Biomech Eng 1980;102:73-84.

15. Lai WM, Mow VC. Drag-induced compression of articular cartilage during a permeation experiment. Biorheology 1980;17:111-23.

16. Mow VC, Gibbs MC, Lai WM, Zhu WB, Athanasiou KA. Biphasic indentation of articular cartilage-II. A numerical algorithm and an experimental study. J Biomech 1989;22:853-61.

17. Mow VC, Ratcliffe A, Poole AR. Cartilage and diarthrodial joints as paradigms for hierarchical materials and structures. Biomaterials 1992;13:67-97.

18. Mow VC, Holmes MH, Lai WM. Fluid transport and mechanical properties of articular cartilage: a review. J Biomech 1984;17:377-94.

19. Clarke IC. Articular cartilage: a review and scanning electron microscope study. 1. The interterritorial fibrillar architecture. J Bone Joint Surg Br 1971;53:732-50.

20. Clark JM. Variation of collagen fiber alignment in a joint surface: a scanning electron microscope study of the tibial plateau in dog, rabbit, and man. J Orthop Res 1991;9:246-57.

21. Muir H, Bullough P, Maroudas A. The distribution of collagen in human articular cartilage with some of its physiological implications. J Bone Joint Surg Br 1970;52:554-63.

22. Broom ND, Marra DL. Ultrastructural evidence for fibril-to-fibril associations in articular cartilage and their functional implication. J Anat 1986;146:185-200.

23. Redler I, Mow VC, Zimny ML, Mansell J. The ultrastructure and biomechanical significance of the tidemark of articular cartilage. Clin Orthop Rel Res 1975;112:357-62.

24. Wang CC-B, Hung CT, Mow VC. An analysis of the effects of depth-dependent aggregate modulus on articular cartilage stress-relaxation behavior in compression. J Biomech 2001;34:75-84.

25. Wang CC, Guo XE, Sun D, Mow VC, Ateshian GA, Hung CT. The functional environment of chondrocytes within cartilage subjected to compressive loading: a theoretical and experimental approach. Biorheology 2002;39:11-25.

26. Schinagl RM, Ting MK, Price JH, Sah RL. Video microscopy to quantitate the inhomogeneous equilibrium strain within articular cartilage during confined compression. Ann Biomed Eng 1996;24:500-12.

27. Schinagl RM, Gurskis D, Chen AC, Sah RL. Depth-dependent confined compression modulus of full-thickness bovine articular cartilage. J Orthop Res 1997;15:499-506.

28. Krishnan R, Park S, Eckstein F, Ateshian GA. Inhomogeneous cartilage properties enhance superficial insterstitial fluid support and frictional properties, but do not provide a homogeneous state of stress. J Biomech Eng 2003;125:569-77.

29. Oettmeier R, Abendroth K, Oettmeier S. Analyses of the tidemark on human femoral heads. II. Tidemark changes in osteoarthrosis - a histological and histomorphometric study in non-decalcified preparations. Acta Morphol Hung 1989;37:169-80.

30. Dequeker J, Mokassa L, Aerssens J, Boonen S. Bone density and local growth factors in generalized osteoarthritis. Microsc Res Tech 1997;37:358-71.

31. Sokoloff L. Microcracks in the calcified layer of articular cartilage. Arch Pathol Lab Med 1993;117:191-5.

32. Mori S, Harruff R, Burr DB. Microcracks in articular calcified cartilage of human femoral heads. Arch Pathol Lab Med 1993;117:196-8.

33. Burr DB, Radin EL. Microfractures and microcracks in subchondral bone: are they relevant to osteoarthrosis? Rheum Dis Clin North Am 2003;29:675-85.

34. Berry JL, Thaeleroberdoerster DA, Greenwald S. Subchondral pathways to the superior surface of the human talus. Foot & Ankle 1986;7:2-9.

35. Holmdahl DE, Ingelmark BE. The contact between the articular cartilage and the medullary cavities of the bone. Acta Orthop Scand 1950;20:156-65.

36. Boyde A, Firth EC. Articular calcified cartilage canals in the third metacarpal bone of 2-year-old thoroughbred racehorses. J Anat 2004;205:491-500.

37. Suh JK, Li Z, Woo SL-Y. Dynamic behavior of a biphasic cartilage model under cyclic compressive loading. J Biomech 1995;28:357-64.

38. Mow VC, Bachrach NM, Ateshian GA. The effects of a subchondral bone perforation on the load support mechanism within articular cartilage. Wear 1994;175:167-75.

39. Grodzinsky AJ, Frank EH. Electromechanical and physicochemical regulation of cartilage strength and metabolism. In: Hukins DWL, ed. Connective tissue matrix: volume II Topics in molecular and structural biology. Boca Raton: CRC Press; 1990:91-126.

40. Chen AC, Bae WC, Schinagl RM, Sah RL. Depth- and strain-dependent mechanical and electromechanical properties of full-thickness bovine articular cartilage in confined compression. J Biomech 2001;34:1-12.

41. Kwan MK, Lai WM, Mow VC. A finite deformation theory for cartilage and other soft hydrated connective tissues - I. equilibrium results. J Biomech 1990;23:145-55.

42. Kwan MK, Hacker SA, Woo SL-Y, Wayne JS. The effect of storage on the biomechanical behavior of articular cartilage-a large strain study. J Biomech Eng 1992;114:149-53.

43. Lai WM, Mow VC, Roth V. Effects of nonlinear strain-dependent permeability and rate of compression on the stress behavior of articular cartilage. J Biomech Eng 1981;103:61-6.

44. Frank EH, Grodzinsky AJ. Cartilage electromechanics-II. A continuum model of cartilage electrokinetics and correlation with experiments. J Biomech 1987;20:629-39.

45. Lee RC, Frank EH, Grodzinsky AJ, Roylance DK. Oscillatory compressional behavior of articular cartilage and its associated electromechanical properties. J Biomech Eng 1981;103:280-92.

46. Maroudas A. Physicochemical properties of cartilage in the light of ion exchange theory. Biophys J 1968;8:575-95.

47. Holmes MH, Lai WM, Mow VC. Singular perturbation analysis of the nonlinear, flow-dependent compressive stress relaxation behavior of articular cartilage. J Biomech Eng 1985;107:206-18.

48. Gu WY, Mao XG, Rawlins BA, et al. Streaming potential of human lumbar anulus fibrosus is anisotropic and affected by disc degeneration. J Biomech 1999;32:1177-82.

49. Gu WY, Lai WM, Mow VC. Transport of fluid and ions through a porous-permeable charged-hydrated tissue, and streaming potential data on normal bovine articular cartilage. J Biomech 1993;26:709-23.

50. Gu WY, Lai WM, Mow VC. A mixture theory for charged-hydrated soft tissues containing multi-electrolytes: passive transport and swelling behaviors. J Biomech Eng 1998;120:169-80.

51. Holmes MH, Mow VC. The nonlinear characteristics of soft gels and hydrated connective tissue in ultrafiltration. J Biomech 1990;23:1145-56.

52. Maroudas A. Transport of solutes through cartilage: permeability to large molecules. J Anat 1976;122:335-47.

53. Ateshian GA, Lai WM, Zhu WB, Mow VC. An asymptotic solution for the contact of two biphasic cartilage layers. J Biomech 1994;27:1347-60.

54. Armstrong CG, Lai WM, Mow VC. An analysis of the unconfined compression of articular cartilage. J Biomech Eng 1984;106:165-73.

APPENDIX A

THEORETICAL ANALYSES

A.1 Large Strain Finite Deformation Model [1]

Cartilage is modeled as a biphasic material, consisting of a porous and permeable elastic solid filled with water [1]. The experimental data were analyzed using a biphasic large strain theory [2]. This large strain theory is an extension of the linear biphasic theory and incorporates strain dependent porosity and permeability in addition to large strains [3]. Using the principles of conservation of mass and energy, equation of continuity, and the assumption of isotropy, the constitutive laws for the apparent solid and fluid stresses are [1]:

$$\sigma^{s} = -\alpha p \mathrm{I} + 2\mathrm{B}\rho \frac{\partial \mathrm{A}}{\partial \mathrm{B}} \quad (\mathrm{A.1})$$

$$\sigma^{f} = -p\mathrm{I} - 2\rho^{f} \left\{ \rho \frac{\partial \mathrm{A}}{\partial \rho^{f}} \right\} \mathrm{I} \quad (\mathrm{A.2})$$

Where the superscripts *s* and *f* refer to solid and fluid respectively. B is the left Cauchy-Green strain tensor, A the Helmholtz free energy function, I the identity tensor, *p* the apparent fluid pressure, α the ratio of solid volume, *ρ* the density of the solid-fluid mixture, ρ^{f} the apparent density of the fluid. With the assumption of isotropy, A becomes a function of the variants of B (i.e., *J1, J2, J3*) thus reducing Eqns. (A.1)-(A.2) to [1]:

$$\sigma^{s} = -\alpha p\mathrm{I} + 2\rho\left\{\left[J_{2}\frac{\partial \mathrm{A}}{\partial J_{2}} + J_{3}\frac{\partial \mathrm{A}}{\partial J_{3}}\right]\mathrm{I} + \frac{\partial \mathrm{A}}{\partial J_{1}}\mathrm{B} - J_{3}\frac{\partial \mathrm{A}}{\partial J_{2}}\mathrm{B}^{-1}\right\} \text{ (A.3)}$$

$$\sigma^{f} = -p\mathrm{I} \text{ (A.4)}$$

The Helmholtz free energy function, A, is chosen as [1]:

$$\mathrm{A} = \frac{1}{8\rho_{0}J_{3}}\left\{(3\lambda_{s} + 2\mu_{s})J_{1} + (\lambda_{s} + 2\mu_{s})J_{1}^{2} - (9\lambda_{s} + 10\mu_{s})J_{2}\right\} \text{ (A.5)}$$

λ_s and μ_s are Lamé constants. Substituting Eqn. (A.5) into Eqn. (A.3) we get [1]:

$$\sigma^{s} = -\alpha p\mathrm{I} + \frac{\rho}{4\rho_{0}J_{3}}\left\{-\left[(3\lambda_{s} + 2\mu_{s})J_{1} + (\lambda_{s} + 2\mu_{s})J_{1}^{2}\right]\mathrm{I} + \left[3\lambda_{s} + 2\mu_{s} + 2(\lambda_{s} + 2\mu_{s})J_{1}\right]\mathrm{B} + (9\lambda_{s} + 10\mu_{s})J_{3}\mathrm{B}^{-1}\right\} \text{ (A.6)}$$

The corresponding equilibrium stress-strain relationship corresponding to the Helmholtz free energy Eqn. (A.5) can also be written as [1]:

$$\sigma_{z} = \frac{1}{4}(\lambda_{s} + 2\mu_{s})\left[1 + d_{1}(\lambda_{3} - 1)\right]\frac{1}{\lambda_{3}}\left[\lambda_{3}^{2} - \frac{1}{\lambda_{3}^{2}}\right] \text{ (A.7)}$$

The *z* subscript refers to the direction of the applied load in confined compression, or the *z*-direction. λ_3 is the stretch in the direction of the compressive load and is related to the strain term [1]:

$$\lambda - 1 = \frac{\partial u}{\partial z} \quad \text{(A.8)}$$

$d_1 = d_0(\alpha_0+1)/(\alpha_0+d_0)$ and α_0 and d_0 are initial solid content and fluid-to-solid true density ratio. The average value of α_0 is around 0.20 [3]. The value of d_0 is estimated to be between 0.70 and 0.90, based on tissue composition, densities of Type II collagen, proteoglycan aggregates and monomers, chondrocytes and other glycoproteins. For our models, we used a value of $d_1 = 0.9$ [2, 4].

The Lamé constants, λ_s and μ_s, are related to the aggregate modulus, H_A, by [1]

$$H_A = \lambda_s + 2\mu_s \quad \text{(A.9)}$$

The sum of Eqn. (A.7) and Eqn. (A.4) represents the total stress experienced by the cartilage. For confined compression where strain is unidirectional, the total stress at equilibrium in the direction of the applied load, or along the *z*-direction, is [1]:

$$\sigma_z = \frac{H_{A0}}{4}\left[1 + 0.9\frac{du}{dz}\right]\left[\frac{\left(1+\frac{du}{dz}\right)^4 - 1}{\left(1+\frac{du}{dz}\right)^3}\right] \quad \text{(A.10)}$$

By using a non-linear least squares regression procedure, Eqn. (A.10) can be used to fit our experimental stress-strain data to obtain an estimate of the aggregate compression modulus, H_A, at each compressive offset level. The aggregate modulus at zero strain, H_{A0}, in this case corresponds to the initial slope of the nonlinear stress-strain curve. By taking the derivative of Eqn. (A.10) with respect to ε or $-du/dz$ we obtain the tangent modulus [1]:

$$\frac{\partial \sigma_z}{\partial \varepsilon} = H_{A0}\left(1-0.9\varepsilon\right) - \frac{3H_{A0}\left(1-0.9\varepsilon\right)\left(\left(1-\varepsilon\right)^4-1\right)}{4\left(1-\varepsilon\right)^4} + 0.225H_{A0}\frac{\left(1-\varepsilon\right)^4-1}{\left(1-\varepsilon\right)^3} \quad \text{(A.11)}$$

The tangent modulus allows us to obtain the aggregate modulus at specific offset strains, including at zero strain, H_{A0} [1]:

$$H_A(i) = \frac{\partial \sigma}{\partial \varepsilon}\left(1-\varepsilon(i)\right) \quad \text{(A.12)}$$

A.2 Multi-Layer Modelling [5]

Frank approximated an inhomogeneous material with smoothly varying properties by overlaying individual homogeneous layers [5]. He approximated spatial variation in cartilage composition and material properties by a series of uniform layers each with its own set of mechanical and electrical parameters. The layers are then spliced together via appropriate boundary conditions to yield the total electromechanical response. Frank showed that the mechanics of each layer could be described by a transfer relation expressed in terms of stress and displacement boundary conditions. The mechanical response of the multiple layer composition is the product of the individual transfer relation matrices.

The total compressive stress is the sum of the fluid pressure, P_f, and the matrix swelling pressure, p:

$$\sigma = p + P_f \quad \text{(A.13)}$$

where the matrix swelling pressure, p, is defined by:

$$p = H_A \varepsilon + \beta \quad \text{(A.14)}$$

The compressive stress, σ, and strain, ε, are defined positive in compression. H_A is the equilibrium confined compression modulus. β represents the swelling stresses at zero strain.

The uniaxial compressive strain is related to the tissue displacement *u(z)* by:

$$\varepsilon = -\frac{\partial u(z)}{\partial z} \quad \text{(A.15)}$$

The equations of continuity, conservation of momentum, electrokinetic coupling, and conservation of current take the form, respectively:

$$\frac{\partial U}{\partial z} = \frac{\partial \varepsilon}{\partial t} \quad \text{(A.16)}$$

$$\frac{\partial \sigma}{\partial z} = 0 \quad \text{(A.17)}$$

$$\begin{bmatrix} U(z) \\ J(z) \end{bmatrix} = \begin{bmatrix} -k_{11} & k_{12} \\ k_{21} & -k_{22} \end{bmatrix} \frac{\partial}{\partial z} \begin{bmatrix} P_f(z) \\ V(z) \end{bmatrix} \quad \text{(A.18)}$$

$$\frac{\partial J}{\partial z} = 0 \quad \text{(A.19)}$$

where *U* is the relative fluid velocity, *J* the current density and *V* the electric potential.

Combining Eqns. (A.13)-(A.19) an equation of motion is obtained for uniaxial displacement, *u(z)*, with a cartilage disk of thickness *δ*. For a single homogeneous layer with uniform ionic concentrations and material properties, the equation of motion is:

$$\frac{\partial u}{\partial t} = H_A k \frac{\partial^2 u}{\partial z^2} + k_i J + U_0 \quad \text{(A.20)}$$

k_iJ represents the electroosmotic fluid flow induced by the current J. U_0 is the constant of integration and represents a divergence-free fluid flow through the tissue. k, the hydraulic permeability, is defined as $k = k_{11} - (k_{12}k_{21}/k_{22})$ and $k_i = k_{12}/k_{22}$ from Eqn. (A.18).

Sinusoidal steady state displacements take the form:

$$u(z,t) = \mathrm{Re}\left\{\hat{u}(z,\omega)e^{j\omega t}\right\} \quad \text{(A.21)}$$

where $\hat{u}$ is the complex amplitude. The equation of motion, Eqn. (A.20), can be transformed into the complex frequency domain as

$$j\omega\hat{u} = H_A k \frac{\partial^2 \hat{u}}{\partial z^2} + k_i \hat{J} + \hat{U}_0 \quad \text{(A.22)}$$

where J and U have the same sinusoidal steady state form as Eqn. (A.21). The chemical stress term, β, is not included in Eqn. (A.22) because there is no equivalent sinusoidal component in β. The “^” notation for complex amplitudes will now be dropped since the remainder of the derivation will deal only with the sinusoidal steady state.

A general solution to the complex equation of motion, Eqn. (A.22), is given by

$$u(z) = \frac{(u^{\alpha} - u_J)\sinh\gamma(\delta - z) + (u^{\beta} - u_J)\sinh\gamma z}{\sinh\gamma\delta} + u_J \quad \text{(A.23)}$$

where

$$u^{\alpha} = u(z=0) \text{ and } u^{\beta} = u(z=\delta)$$

are the displacement amplitudes imposed at the top (α) and bottom (β) surfaces of the tissue and

$$u_J = \frac{k_i J + U_0}{j\omega} \quad \text{(A.24)}$$

$$\gamma^2 = \frac{j\omega}{H_A k_p} \quad \text{(A.25)}$$

u_J is the displacement produced from current generation.

By solving Eqn. (A.15) for strain using Eqn. (A.23), we get:

$$\varepsilon = -\frac{\partial u}{\partial z} = -\left[\frac{-\gamma(u^{\alpha} - u_J)\cosh\gamma(\delta - z) + \gamma(u^{\beta} - u_J)\cosh\gamma z}{\sinh\gamma\delta}\right] \quad \text{(A.26)}$$

$$= \gamma\left[\frac{(u^{\alpha} - u_J)\cosh\gamma(\delta - z) - (u^{\beta} - u_J)\cosh\gamma z}{\sinh\gamma\delta}\right] \quad \text{(A.27)}$$

From Eqn. (A.14), where it is assumed β is zero, the fluid pressure can be determined:

$$p(z) = H_A\varepsilon = H_A\gamma\frac{(u^{\alpha} - u_J)\cosh\gamma(\delta - z) - (u^{\beta} - u_J)\cosh\gamma z}{\sinh\gamma\delta} \quad \text{(A.28)}$$

We know $\sigma = H_A \varepsilon + P_f$ and set $P_f = 0$ by using one or two porous permeable platen(s) in our testing setup:

$$\sigma = H_A \gamma \left[\frac{(u^\alpha - u_J)\cosh \gamma(\delta - z) - (u^\beta - u_J)\cosh \gamma z}{\sinh \gamma\delta} \right] \quad \text{(A.29)}$$

At $z = 0$:

$$p^\alpha = H_A \gamma \frac{(u^\alpha - u_J)\cosh \gamma\delta - (u^\beta - u_J)}{\sinh \gamma\delta} \quad \text{(A.30)}$$

At $z = \delta$:

$$p^\beta = H_A \gamma \frac{(u^\alpha - u_J) - (u^\beta - u_J)\cosh \gamma\delta}{\sinh \gamma\delta} \quad \text{(A.31)}$$

The pressures, p^α and p^β, at the top and bottom surfaces, respectively, can now be written in terms of a transfer relation matrix and the boundary displacements:

$$\begin{bmatrix} p^\alpha \\ p^\beta \end{bmatrix} = H_A \gamma \begin{bmatrix} \coth \gamma\delta & \dfrac{-1}{\sinh \gamma\delta} \\ \dfrac{1}{\sinh \gamma\delta} & -\coth \gamma\delta \end{bmatrix} \begin{bmatrix} u^\alpha - u_J \\ u^\beta - u_J \end{bmatrix} \quad \text{(A.32)}$$

Eqn. (A.20) can be re-written to obtain an equivalent matrix that relates the top (α) surface values to the bottom (β) surface values:

$$\begin{bmatrix} p^{\alpha} \\ u^{\alpha} \end{bmatrix} = \begin{bmatrix} \cosh \gamma\delta & H_A \gamma \sinh \gamma\delta \\ \dfrac{\sinh \gamma\delta}{H_A \gamma} & \cosh \gamma\delta \end{bmatrix} \begin{bmatrix} p^{\beta} \\ u^{\beta} \end{bmatrix} + \begin{bmatrix} -H_A \gamma \sinh \gamma\delta \\ 1 - \cosh \gamma\delta \end{bmatrix} u_J \quad \text{(A.33)}$$

For a tissue model of *n* layers, there are *n*+1 interfaces. The general i^{th} layer is bounded by top interface *i*-1 and bottom interface *i*. Parameters related to the i^{th} layer or i^{th} interface will be designated by a superscript *i*. Applying Eqn. (A.21) to the i^{th} layer:

$$\begin{bmatrix} p^{i-1} \\ u^{i-1} \end{bmatrix} = \mathrm{A}^i \begin{bmatrix} p^i \\ u^i \end{bmatrix} + \left[\mathrm{I} - \mathrm{A}^i\right] \begin{bmatrix} 0 \\ u_J^i \end{bmatrix} \quad \text{(A.34)}$$

where A^{i} is the 2x2 matrix for the i^{th} layer and I is the identity matrix. At each interface the displacement and swelling stress is continuous; that is, the displacement and swelling stress at the bottom of the i^{th} layer is identical to that of the top of the $i+1^{st}$ layer. Thus we can splice together the layers by multiplying the matrices for all the layers together:

$$\begin{bmatrix} p^0 \\ u^0 \end{bmatrix} = \Pi^n \begin{bmatrix} p^n \\ u^n \end{bmatrix} + \sum_{i=1}^{n} \left[\Pi^{i-1} - \Pi^i\right] \begin{bmatrix} 0 \\ u_J^i \end{bmatrix} \quad \text{(A.35)}$$

p^0 and u^0 are the swelling stress and displacement at $z = 0$ (the surface), and the $\Pi -$ matrix is defined as

$$\Pi^i = \prod_{j=0}^{i} \mathrm{A}^j \quad \text{(A.36)}$$

and

$$\Pi^0 = A^0 = I \quad \text{(A.37)}$$

For confined compression setup configurations 1 and 2, the sample is constrained below by a no displacement condition and there is no fluid flow being applied to our samples during testing, thus $u^n = 0$ and $U_0 = 0$ everywhere. Above the sample, fluid may flow freely through a porous platen so that $P_f = 0$. For these boundary conditions, the total stress σ can be evaluated directly from Eqn. (A.35) as $\sigma = p^0$.

$$\sigma = \frac{\Pi_{11}^n}{\Pi_{21}^n} u^0 + \sum_{i=1}^{n} \frac{\Pi_{21}^n(\Pi_{12}^{i-1} - \Pi_{12}^i) - \Pi_{11}^n(\Pi_{22}^{i-1} - \Pi_{22}^i)}{\Pi_{21}^n} u_J^i \quad \text{(A.38)}$$

Under open circuit conditions, $J = 0$ and Eqn. (A.38) reduces to:

$$\sigma = \Lambda u^0 \quad \text{(A.39)}$$

where the dynamic stiffness, Λ_C, is defined as:

$$\Lambda_C = \frac{\Pi_{11}^n}{\Pi_{21}^n} \quad \text{(A.40)}$$

A.3 References

1. Kwan MK, Lai WM, Mow VC. A finite deformation theory for cartilage and other soft hydrated connective tissues - I. equilibrium results. J Biomech 1990;23:145-55.

2. Kwan MK, Hacker SA, Woo SL-Y, Wayne JS. The effect of storage on the biomechanical behavior of articular cartilage-a large strain study. J Biomech Eng 1992;114:149-53.

3. Mow VC, Kuei SC, Lai WM, Armstrong CG. Biphasic creep and stress relaxation of articular cartilage in compression: theory and experiment. J Biomech Eng 1980;102:73-84.

4. Schinagl RM, Gurskis D, Chen AC, Sah RL. Depth-dependent confined compression modulus of full-thickness bovine articular cartilage. J Orthop Res 1997;15:499-506.

5. Frank EH, Grodzinsky AJ. Cartilage electromechanics-II. A continuum model of cartilage electrokinetics and correlation with experiments. J Biomech 1987;20:629-39.

APPENDIX B

THE ROLES OF DEPTH VARYING MECHANICAL PROPERTIES AND PERMEABILITY OF THE DEEP BOUNDARY CONDITION IN CONFINED COMPRESSION OF ARTICULAR CARTILAGE – EXPERIMENTAL RESULTS

B.1 Abstract

The objective of this study was to define the roles of depth varying mechanical properties of articular cartilage and the permeability of the deep boundary condition in the time-dependent and dynamic biomechanical responses of cartilage. The study utilized two types of specimens: a full thickness cartilage sample with normal depth varying mechanical properties and relatively homogeneous cartilage samples consisting of four 250 μm slices of cartilage taken from the middle or deep zones of different osteochondral cores. These samples were tested in two confined compression setups, both with a permeable platen applying displacement on top and either a permeable or impermeable deep boundary condition, and were subjected to stress relaxation and oscillatory compression tests at 15 and 25% compression offsets. Results show that homogeneous cartilage has decreased fluid pressurization capability compared to inhomogeneous cartilage evidenced by shorter stress relaxation times, decreased dynamic stiffness and an increased phase difference between applied

dynamic displacement and solid surface stress in oscillatory compression. This suggests homogeneous cartilage experiences increased friction between the solid matrix and interstitial fluid in addition to deeper solid matrix strain leading to progressive cartilage wear and degeneration. These results are accentuated when the deep boundary condition, representing the subchondral bone plate, becomes permeable to fluid. In summary, the inhomogeneity of cartilage enhances fluid pressurization, protecting the solid matrix of cartilage from wear and tear seen in the homogeneous samples with this effect amplified with a permeable subchondral bone plate interface.

B.2 Methods

I. Sample Preparation

Bovine osteochondral samples were harvested and mechanical testing of the articular cartilage samples were performed using methods described previously [1-3]. Four osteochondral blocks were isolated from the medial patellofemoral groove of each of four adult bovine knee joints obtained shortly after slaughter (Tip Top Meats, Carlsbad, CA) and were immediately processed to obtain thirty full-thickness osteochondral cores using a 6.4 mm diameter core drill. During the explant procedure, cartilage was kept moist and free of blood by irrigation with sterile phosphate-buffered saline (PBS) supplemented with proteinase inhibitors (PI) (1 mM phenylmethylsulfonyl fluoride, 2 mM EDTA, 5 mM benzamidine-HCl, and 10 mM N-ethylmaleimide). These cores were then individually stored in vials with PBS+PI at -20°C until further processing.

II. Sample Types (Figure B.1A)

The cartilage from the thirty osteochondral cores were microtomed (Microm, Germany) parallel to the articular surface at 250 μm increments from the surface until reaching the subchondral bone yielding four to seven slices. The slices were individually vialed in PBS+PI and labeled by core number and depth order from superficial to deep. Six cartilage cores were used to create full-thickness samples (FT) by restacking the slices from the same core in their original order and orientation. The remaining twenty-four cores were used to construct the homogeneous middle-zone (MZ) and homogeneous deep-zone (DZ) sample types. Six MZ samples were constructed by taking the middle two slices of twelve cores and stacking two pairs of them to create four slice MZ samples. If a cartilage core had an even number of slices, the middle two slices were chosen. If the cartilage core had an odd number of slices, the middle two slices nearer the articular surface were chosen. The top two paired slices had the articular surface facing sides pointing upwards and the bottom two slices had the articular surface facing sides pointing downwards. Six DZ samples were constructed by taking the deepest slice from twenty four separate cores and stacking four of them with the top two slices having their articular facing surface sides pointing upwards and the bottom two slices having their articular facing surface sides pointing downwards.

Thicknesses of the samples were measured using a mechanical spectrometer (DynaStat, IMASS, Accord, MA) after applying a 10 g equalized load to hold the sample slices together.

III. Confined Compression Testing (Figure B.1B)

Each sample was thawed in PBS+PI at room temperature (22°C) prior to mechanical testing. Each sample was subjected to confined compression testing using two configurations (I and II; Figure B.1B) applying randomly either a non-permeable or permeable boundary condition on the bottom side of the sample. Both confined compression testing chambers were filled with PBS+PI so that the sample was soaked in PBS+PI during the entirety of the test. The articular surface of each sample was loaded with a rigid, porous, stainless-steel frit (0.5 μm porosity) and the bottom of the specimen was placed on either an impermeable base for configuration I or a rigid, porous, stainless-steel frit (0.5 μm porosity) for configuration II. Automated electromechanical testing and data acquisition were implemented by interfacing a computer-controlled function generator (HP33120A, Hewlett-Packard, Palo Alto, CA) to the mechanical spectrometer. The load and displacement signals from the spectrometer were captured within a personal computer (Macintosh IIvx, Apple Computer, Inc., Cupertino, CA) running LabView software (National Instruments, Austin, TX).

The test sequence consisted of applying a 400 second, 0-15% ramp compression (0.0375%/sec) and allowing the load to relax in 2800 seconds. This duration is sufficient to achieve >95% equilibration for a cartilage sample that is 1.125 mm thick and has material properties of H_{A0} = 0.45 MPa, k_{p0} = 1.4 x 10-15 m^2/Pas, and a characteristic time constant of ~700 seconds [1, 4]. This was followed by a series of three full oscillatory compressions at each of the following frequencies of 0.01, 0.02, 0.05, 0.1, 0.2 and 0.5 Hz with respective amplitudes of 0.3, 0.26, 0.22, 0.18, 0.14 and 0.1% (of compression offset thickness). This was followed by another 400 sec, 15-25% ramp compression (0.025%/sec) with 2800 sec of relaxation time and followed by the same oscillatory compression series. At each frequency, the response was averaged over the three oscillation cycles for dynamic analysis. These compression amplitudes were chosen so that the oscillatory strains were small (computed to be $\leq$ 10%) everywhere within the tissue according to theoretical analysis using the homogeneous model [2].

Time between repeated testing (randomized) was at least 1 hr, and PBS+PI was used as the bathing solution at all times.

IV. Fitting of Data for Estimating Material Properties

Using the equilibrium and oscillatory data from osteochondral cores, mechanical material properties were estimated using a homogeneous model. From the equilibrium data, H_{A0} was estimated by fitting the finite deformation constitutive relationship to the experimental data using a least-squares method [4, 6, 7]. The finite deformation relationship fit the data well with $r^2 = 0.985 \pm 0.032$. The strain-dependent permeability values were estimated using a continuum model described previously for a homogeneous sample [6]. This was done by fitting the homogeneous continuum model to the oscillatory displacement and load data at each offset compression level using the H_{A0} value obtained from the equilibrium data.

V. Data Analysis and Statistics

Data analysis was performed using Excel 2003 (Microsoft, Bellevue, WA). Stress-relaxation curves were normalized to equilibrium stress (Figure B.3). The effects of sample type (FT, MZ, DZ) and testing setup (I, II) on normalized peak load ratio, 50% relaxation time constant (τ_{50}), compressive modulus (H_{A0}), permeability (k_{p0}), and dynamic stiffness and phase were assessed using separate repeated-measures

ANOVA ($\alpha<0.05$) with pairwise comparison of sample types. The Tukey post hoc test was used for multiple comparisons. All statistical analyses were done using SYSTAT 10.2 (Systat, Evanston, IL). Data are expressed as mean ± SD.

B.3 Results

Sample thicknesses were 1.29 ± 0.16 mm, 1.10 ± 0.08 mm, and 1.08 ± 0.05 mm for FT, MZ and DZ groups respectively.

Equilibrium stress varied in a sample dependent manner with this dependence pronounced at the higher offset strain. The equilibrium stresses for all three sample types did not vary with setup at each strain offset. At 25% strain offset, DZ samples had ~55% higher equilibrium stress than all other sample types.

Stress relaxation time constants, $\tau 50$, (Figure B.2) varied with testing configuration ($p < 0.001$), in a sample-dependent manner (interaction $p < 0.001$). $\tau 50$ for FT samples, did not vary with testing configuration. MZ and DZ had ~21% and ~41% lower relaxation times in setup II than in I at strain offsets of 15 and 25% respectively. In setup I, $\tau 50$ increased for DZ samples ($p < 0.05$). At 25% offset, MZ and DZ samples in setup II had ~25% lower $\tau 50$ than FT samples (each $p < 0.05$).

Normalized peak stresses (Figure B.3) were ~40% lower in setup II than in I ($p < 0.001$) and tended to vary with sample type ($p = 0.08$). Normalized peak stresses for MZ and DZ samples were 47% and 43% lower in setup II than in I at 25% offset and ~40% and ~28% at 15% offset. MZ and DZ samples had ~30% lower normalized peak stresses than FT samples in setup II (each $p < 0.001$) but not in setup I. Normalized peak stresses for FT samples did not vary with testing configuration.

Dynamic stiffness (Figure B.4A-C) increased with frequency ($p < 0.001$) and was greater for setup I ($p < 0.01$) throughout the frequency range. Dynamic stiffness also saw an interaction between sample type and configuration. At both strain offsets, the dynamic stiffness in each setup for FT samples tended to diverge at higher frequencies. Phase angle decreased with frequency ($p < 0.001$) in a sample and setup-dependent manner (interaction $p < 0.001$) evident by a diminishing difference with frequency and by reversal of trend of setup I having greater phase angle for MZ and DZ sample (Figure B.4EF). In setup II, phase angles for MZ and DZ samples were higher than FT samples throughout the frequency range.

B.4 Discussion

The roles of depth varying mechanical properties of articular cartilage and the subchondral bone plate in cartilage biomechanics are not completely understood. Our experimental and computational results provide evidence that the depth varying inhomogeneity of articular cartilage protects the tissue's solid matrix from excessive wear and tear when compared to homogeneous constructs. The impermeability of the subchondral bone plate further protects cartilage by increasing load bearing by fluid pressurization, relieving the solid matrix from excessive stresses that occur in joints. This fluid pressurization is enhanced when both elements, the depth varying properties of cartilage and the impermeability of the subchondral bone plate are intact. The experimental studies and model presented here show that the decrease in permeability and the increase in compressive modulus with depth protects the solid matrix, regardless of whether the subchondral bone plate is impermeable or permeable, by maintaining interstitial fluid pressure through its depth. When cartilage becomes homogeneous, as in osteoarthritis, the permeability of the subchondral bone plate may contribute to the degradation process by decreasing fluid pressurization capability.

While our study did not directly test pure homogeneous samples, an attempt was made to recreate homogeneous samples from healthy articular cartilage by taking slices from equivalent zones by depth from several osteochondral cores and stacking them. The deep zone homogeneous samples tended to have higher equilibrium stresses and longer stress relaxation times than the middle zone homogeneous samples (Figure B.2), highlighting the mechanical differences in these two zones. The mechanical properties of cartilage in the superficial zone can vary by more than 10-fold in confined compression moduli and 5-fold in permeability [8-11]. By eliminating this zone in the two homogeneous sample types, the sample becomes considerably more homogeneous. These homogeneous sample types were created by slicing cartilage samples and restacking them for mechanical testing. Theoretically, this should have little impact on mechanical testing. However, slices may slip between each other during oscillations and the abrupt discontinuity of tissue matrix between slices may alter fluid flow characteristics and charge densities. To minimize the impact that this 'slicing effect' may have on differences seen in mechanical testing between homogeneous and inhomogeneous samples, we also sliced full thickness inhomogeneous cartilage samples. Pilot studies have suggested that the slicing effect may be negligible.

Our experimental and model studies utilized a freely permeable deep boundary condition. While not representative of what may occur physiologically, this setup provides insight into the importance of the deep boundary condition permeability in cartilage biomechanics, particularly in time-dependent and dynamic oscillatory compression. The poroelastic model clearly shows that the inhomogeneous sample utilizes maximal fluid pressurization along its depth more so than the homogeneneous sample (Figures 2.4 and 2.5). This becomes important when the deep boundary condition becomes permeable as in setup II when the homogeneous sample loses even more ability to pressurize fluid throughout its depth when compared to the inhomogeneous sample (Figures 2.4CF and 2.5CF). As a result, the stiffness of the homogeneous sample is significantly reduced by about 50% when the deep boundary condition changes from impermeable to permeable (Figure 2.3). However, the inhomogeneous sample, because it is able to maximally pressurize more fluid throughout its depth maintains much of its stiffness and only loses about 17% stiffness at 1 Hz (Figure 2.3) going from impermeable to permeable deep boundary condition. This highlights the functional role that depth varying properties of articular cartilage allow for maximal fluid pressurization throughout its depth. The nonlinear strain dependent permeability of cartilage further supports this functional role [14]. As the soft superficial layer absorbs most of the tissue strain, the solid pores in this region become smaller and the fixed charge density increases, decreasing permeability and essentially trapping fluid beneath this zone, increasing fluid pressurization [5, 12-24].

An increase in hydraulic conductance or a decrease in fluid pressurization capability of osteochondral tissue and the subchondral bone plate may cause progressive deterioration of cartilage. Articular cartilage's low permeability allows it to support large loads through interstitial fluid pressurization, allowing for prolonged load support and minimizing solid matrix strain [25]. The duration of this load support by fluid pressurization to reach equilibrium is characterized by a viscoelastic time constant, τ, which is dependent on the tissue thickness, h, permeability, k, compressive modulus, $H_{A,}$ and it's relationship to these is $\tau = h^2/H_A k$ [54]. For healthy human cartilage with a thickness of 1 cm, compressive modulus, H_A, of 0.5 MPa, and permeability, k_p, of 2 x 10^{-15} m^2/Pa s, the time constant, τ, is 28 hours, a timescale orders of magnitude larger than most physiological situations. With increased hydraulic conductance of both articular cartilage and the subchondral bone plate, an increase of fluid exudation through the subchondral bone plate will lead to shorter equilibrium times and large deformations, accelerating solid matrix degeneration.

B.5 Figures

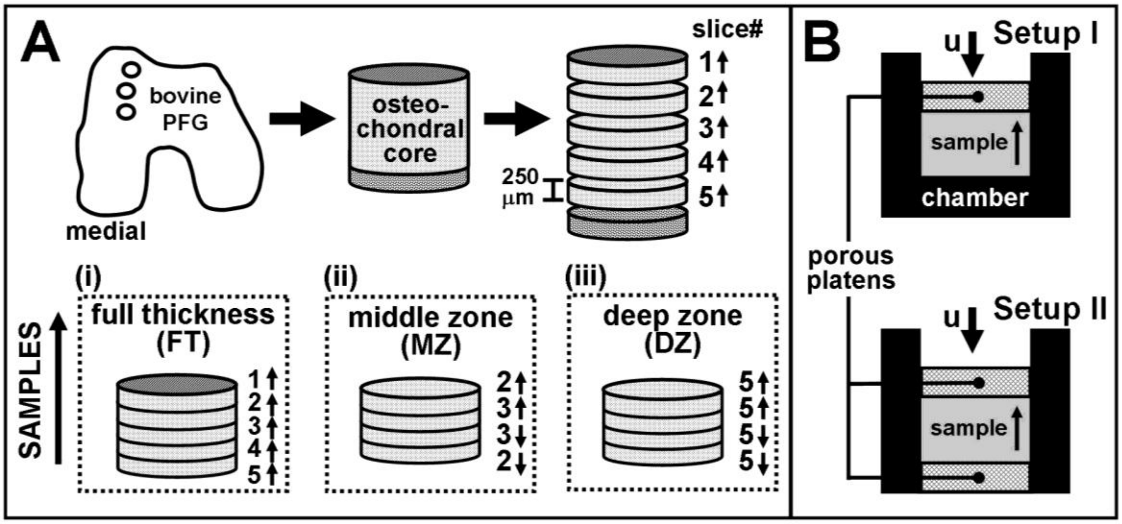

Figure B.1 Sample Types and Confined Compression Setups. (**A**) Osteochondral cores from the medial patellofemoral groove of bovine knees were used to construct three sample types: full thickness (FT, n = 6), middle zone (MZ, n = 6), and deep zone (DZ, n = 6) cartilage samples. Each slice was 250 μm thick. Arrows indicate the direction of articular surface. (**B**) Confined compression testing setup I (1 porous platen) and II (2 porous platens).

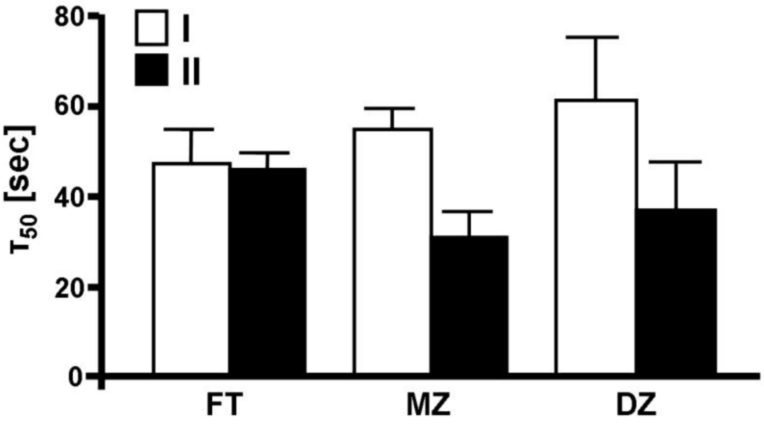

Figure B.2 50% Stress Relaxation Time Constants, τ_{50} [sec], for each sample type and testing configuration at 25% strain offset. Mean + standard deviation. Confined compression setup configurations: open box (I) = one porous platen, filled box (II) = two porous platens. FT = full thickness, n = 6; MZ = middle zone, n = 6; DZ = deep zone, n = 6.

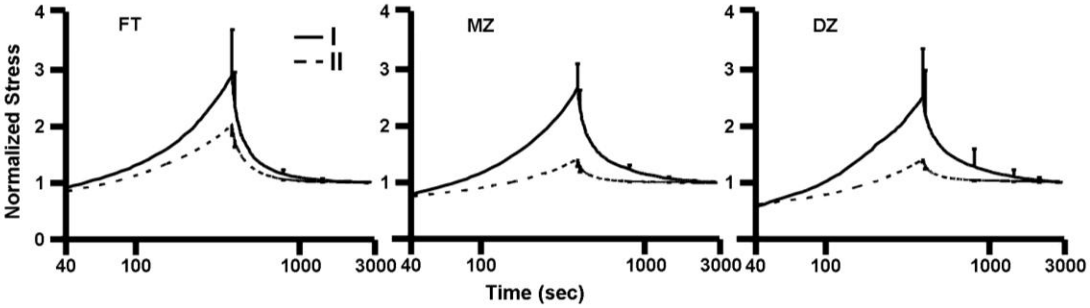

Figure B.3 Normalized Stress Relaxation Curves for each sample type and testing setup configuration at 25% strain offset. Stress curves are normalized to equilibrium stress. Samples were ramped up to 25% strain offset over 400 seconds from an initial strain offset of 15%, a rate of 0.025 %/s. Mean ± standard deviation. Confined compression setup configurations: solid lines (I) = one porous platen, dashed lines (II) = two porous platens. Sample types: FT = full thickness, n = 6; MZ = middle zone, n = 6; DZ = deep zone, n = 6.

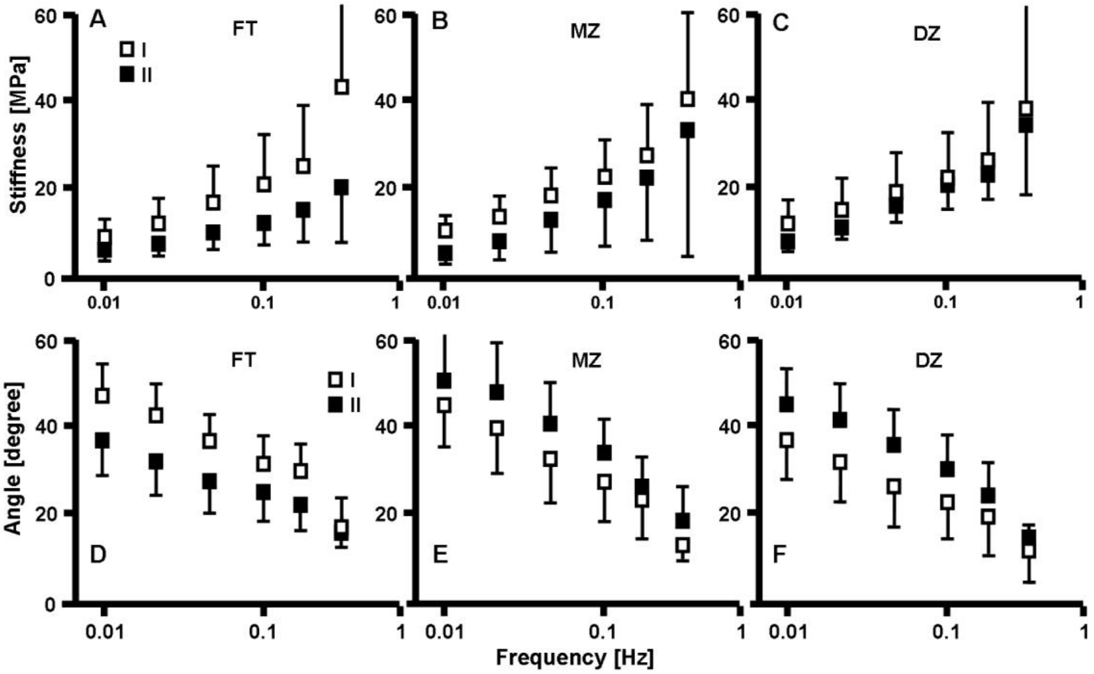

Figure B.4 Dynamic Stiffness [MPa], top row **(A-C)**, and Phase Angle [degree], bottom row **(D-F)**, vs. frequency [Hz] for each sample type and testing setup configuration at 25% strain offset. Mean ± standard deviation. Confined compression setup configurations: open box (I) = one porous platen, filled box (II) = two porous platens. **(A) and (D)** FT = full thickness, n = 6; **(B) and (E)** MZ = middle zone, n = 6; **(C) and (F)** DZ = deep zone, n = 6.

B.6 References

1. Chen AC, Bae WC, Schinagl RM and Sah RL. Depth- and strain-dependent mechanical and electromechanical properties of full-thickness bovine articular cartilage in confined compression. J Biomech 34: 1–12; 2001.

2. Chen AC, Nguyen TT and Sah RL. Streaming potentials during the confined compression creep test of normal and proteoglycan-depleted cartilage. Ann Biomed Eng 25: 269-77; 1997.

3. Frank EH and Grodzinsky AJ. Cartilage electromechanics - II. A continuum model of cartilage electrokinetics and correlation with experiments. J Biomech 20: 629-639; 1987.

4. Schinagl RM, Gurskis D, Chen AC and Sah RL. Depth-dependent confined compression modulus of full-thickness bovine articular cartilage. J Orthop Res 15: 499-506; 1997.

5. Mow VC and Ratcliffe A. Structure and function of articular cartilage and meniscus. Basic Orthopaedic Biomechanics. Ed. Mow VC and Hayes WC. New York: Raven Press. 113-178; 1997.

6. Kwan MK, Hacker SA, Woo SL and Wayne JS. The effect of storage on the biomechanical behavior of articular cartilage - a large strain study. J Biomech Eng 114: 149-153; 1992.

7. Kwan MK, Lai WM and Mow VC. A finite deformation theory for cartilage and other soft hydrated connective tissues – I. Equilibrium results. J Biomech 23: 145-155; 1990.

8. Wang CC, Hung CT and Mow VC. An analysis of the effects of depth-dependent aggregate modulus on articular cartilage stress-relaxation behavior in compression. J Biomech 34: 75–84; 2001.

9. Wang CB, Guo XE, Sun DN, Mow VC, Ateshian GA and Hung CT. The functional environment of chondrocytes within cartilage subjected to compressive loading: A theoretical and experimental approach. Biorheology 39: 11-25; 2002.

10. Schinagl RM, Ting MK, Price JH and Sah RL. Video microscopy to quantitate the inhomogeneous equilibrium strain within articular cartilage during confined compression. Ann Biomed Eng 24: 500–12; 1996.

11. Schinagl RM, Gurskis D, Chen AC and Sah RL. Depth-dependent confined compression modulus of full-thickness bovine articular cartilage. J Orthop Res 15: 499–506; 1997.

12. Maroudas A. Physicochemical properties of articular cartilage. Adult Articular Cartilage. Ed. Freeman MAR. Kent, UK: Pitman Med. 2nd ed: 215–323; 1979.

13. Maroudas A. Physicochemical properties of cartilage in the light of ion exchange theory. Biophys J 8: 575–95; 1968.

14. Mow VC, Kuei SC, Lai WM and Armstrong CG. Biphasic creep and stress relaxation of articular cartilage in compression: theory and experiments. J Biomech Eng 102: 73–84; 1980.

15. Lai WM and Mow VC. Drag-induced compression of articular cartilage during a permeation experiment. Biorheology 17: 111–23; 1980.

16. Mow VC, Gibbs MC, Lai WM, Zhu WB and Athanasiou KA. Biphasic indentation of articular cartilage. II. A numerical algorithm and an experimental study. J Biomech 22: 853–61; 1989.

17. Mow VC, Ratcliffe A and Poole AR. Cartilage and diarthrodial joints as paradigms for hierarchical materials and structures. Biomaterials 13: 67–97; 1992.

18. Mow VC, Holmes MH and Lai WM. Fluid transport and mechanical properties of articular cartilage: a review. J Biomech 17: 377–94; 1984.

19. Holmes MH, Lai WM and Mow VC. Singular perturbation analysis of the nonlinear, flow-dependent compressive stress relaxation behavior of articular cartilage. J Biomech Eng 107: 206–18; 1985.

20. Gu WY, Mao XG, Rawlins BA, Iatridis JC, Foster RJ, Sun DN, Weidenbaum M and Mow VC. Streaming potential of human lumbar annulus fibrosus is anisotropic and affected by disc degeneration. J Biomech 32: 1177–82; 1999.

21. Gu WY, Lai WM and Mow VC. Transport of fluid and ions through a porous permeable charged-hydrated tissue, and streaming potential data on normal bovine articular cartilage. J Biomech 26: 709–23; 1993.

22. Gu WY, Lai WM and Mow VC. A mixture theory for charged-hydrated soft tissues containing multi-electrolytes: passive transport and swelling behaviors. J Biomech Eng 120: 169–80; 1998.

23. Holmes MH and Mow VC. The nonlinear characteristics of soft gels and hydrated connective tissues in ultrafiltration. J Biomech 23: 1145–56; 1990.

24. Maroudas A. Transport of solutes through cartilage: permeability to large molecules. J Anat 122: 335–47; 1976.

25. Ateshian GA, Lai WM, Zhu WB and Mow VC. An asymptotic solution for the contact of two biphasic cartilage layers. J Biomech 27: 1347–60; 1994.